

Calcium dissolution in bridgmanite in the Earth's deep mantle

<https://doi.org/10.1038/s41586-022-05237-4>

Received: 18 December 2020

Accepted: 15 August 2022

Published online: 19 October 2022

 Check for updates

Byeongkwan Ko^{1,8}✉, Eran Greenberg^{2,3}, Vitali Prakapenka², E. Ercan Alp⁴, Wenli Bi^{4,5}, Yue Meng⁶, Dongzhou Zhang^{2,7} & Sang-Heon Shim¹✉

Accurate knowledge of the mineralogy is essential for understanding the lower mantle, which represents more than half of Earth's volume. CaSiO_3 perovskite is believed to be the third-most-abundant mineral throughout the lower mantle, following bridgmanite and ferropericlase^{1–3}. Here we experimentally show that the calcium solubility in bridgmanite increases steeply at about 2,300 kelvin and above 40 gigapascals to a level sufficient for a complete dissolution of all CaSiO_3 component in pyrolite into bridgmanite, resulting in the disappearance of CaSiO_3 perovskite at depths greater than about 1,800 kilometres along the geotherm^{4,5}. Hence we propose a change from a two-perovskite domain (TPD; bridgmanite plus CaSiO_3 perovskite) at the shallower lower mantle to a single-perovskite domain (SPD; calcium-rich bridgmanite) at the deeper lower mantle. Iron seems to have a key role in increasing the calcium solubility in bridgmanite. The temperature-driven nature can cause large lateral variations in the depth of the TPD-to-SPD change in response to temperature variations (by more than 500 kilometres). Furthermore, the SPD should have been thicker in the past when the mantle was warmer. Our finding requires revision of the deep-mantle mineralogy models and will have an impact on our understanding of the composition, structure, dynamics and evolution of the region.

It has been widely accepted that two separate perovskite phases, $(\text{Mg},\text{Fe})(\text{Al},\text{Si})\text{O}$, bridgmanite (Brg) and CaSiO_3 perovskite (CaPv), exist in the lower mantle, together with $(\text{Mg},\text{Fe})\text{O}$ ferropericlase (Fp). This view appears to be supported by experiments where the existence of separate CaPv was found in the mantle-related compositions at the pressure and temperature (*P*–*T*) conditions of the lower mantle^{1–3}. However, some notable exceptions have been reported in many experiments: CaPv was not observed at either higher pressures⁶ or higher temperatures^{7,8} (Extended Data Fig. 1; detailed discussion in Methods). Some experimental⁹ and theoretical^{10–12} studies have shown that the solubility of CaSiO_3 in pure MgSiO_3 Brg increases with increasing temperature, although the suggested solubility is not sufficient for a complete dissolution at the lower-mantle pressures for pyrolite which contains 3.5 wt% calcium oxide (CaO)¹³. However, possible effects from iron (Fe) and aluminium (Al) on the solubility of CaSiO_3 in Brg have not been well explored, despite their considerable amounts in the phase. Recently, a study based on density functional theory combined with molecular dynamics¹² predicted that Fe increases the solubility of CaSiO_3 in Brg, whereas Al decreases it. The theoretical prediction and the ‘missing CaPv’ reported in some previous experiments raise an important question whether all CaSiO_3 can dissolve into Brg and form a single-perovskite phase in the lower mantle.

Stability of Ca-rich bridgmanite

In this study, we investigated the solubility of CaSiO_3 in Brg at lower-mantle-related conditions (33–110 GPa and 1,800–3,000 K) using laser-heated diamond anvil cells (LHDACs) combined with *in situ* X-ray diffraction (XRD). The studied compositions include calcium (Ca)-enriched pyrolytic (Ca-pyrolite), komatiitic and $\text{Ca}_{0.1}\text{Mg}_{0.8}\text{Fe}_{0.1}\text{SiO}_3$ (Ca10Fe10) compositions (see Methods and Extended Data Table 1 for detail). In the Ca-pyrolite composition, we increased the CaSiO_3 content of pyrolite for a better detection of CaPv. The other two compositions have sufficient amounts of CaO. The recovered samples were analysed for mineralogy and chemical composition in scanning-transmission electron microscopy (STEM).

Figure 1a shows two different mineralogy domains identified from our data (Fig. 2a,b): single-perovskite and two-perovskite domains. At 30–40 GPa, two perovskite phases, Brg and CaPv were observed up to 2,400 K (Fig. 1a). At 40–110 GPa, CaPv was clearly identified by multiple lines with strong intensities at temperatures below about 2,300 K. At temperatures above about 2,300 K in the pressure range, however, the XRD peaks of CaPv disappeared, whereas Brg remained with strong peak intensities as a single-perovskite phase (Fig. 2a,b and Extended Data Fig. 2).

¹School of Earth and Space Exploration, Arizona State University, Tempe, AZ, USA. ²Centre for Advanced Radiation Sources, University of Chicago, Chicago, IL, USA. ³Soreq Nuclear Research Centre, Applied Physics Department, Yavne, Israel. ⁴Advanced Photon Source, Argonne National Laboratory, Lemont, IL, USA. ⁵Department of Physics, University of Alabama at Birmingham, Birmingham, AL, USA. ⁶X-ray Science Division, Argonne National Laboratory, Lemont, IL, USA. ⁷School of Ocean and Earth Science and Technology, University of Hawai'i at Manoa, Honolulu, HI, USA. ⁸Present address: Department of Earth and Environmental Sciences, Michigan State University, East Lansing, MI, USA. ✉e-mail: olivine.ko@gmail.com; shdshim@asu.edu

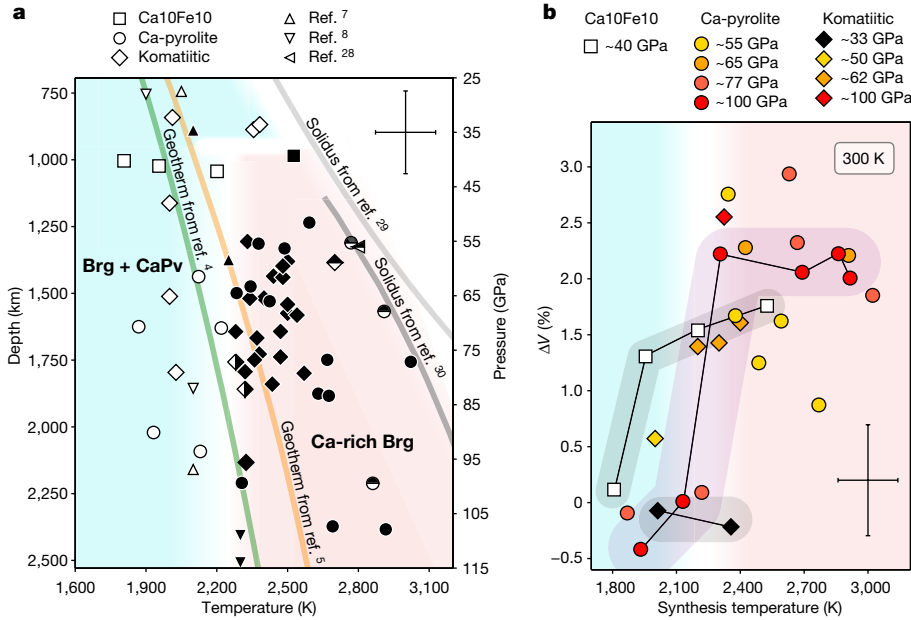


Fig. 1 | Stability of a single-perovskite mineralogy at high pressure–temperature conditions. **a**, In situ XRD observations of perovskite phases. The closed and open symbols represent the observations of a single-perovskite phase (Ca-rich bridgmanite) and two-perovskite phase ($\text{Brg} + \text{CaSiO}_3$ perovskite), respectively (the compositions were measured with STEM). The half-filled symbols denote the presence of CaPv with Ca-rich Brg. Each data point represents a single heating run. Some previous data points on pyrolytic compositions^{7,8,28} are shown with triangle symbols (Methods). The grey lines are the reported solidi of mantle-related compositions^{29,30}. The orange and green curves are the proposed mantle geotherms^{4,5}. The background is shaded with blue and red for the two-perovskite and the single-perovskite domains, respectively. **b**, Change in the unit-cell volumes (ΔV) of Brg as a function of synthesis temperature. The unit-cell volumes of Brg were measured upon temperature quench (300 K) at high pressures and then compared with those expected for Brg observed with CaPv for the corresponding compositions (see Methods for detail). A steep increase in the Brg volume at about 2,300 K indicates a significant increase in the Ca solubility. The black lines connect the Ca10Fe10 data at about 40 GPa, Ca-pyrolite data at about 100 GPa or komatiitic composition data at about 33 GPa, respectively. The shades are a guide for the eye. The error bars are the estimated 1σ uncertainties.

We observed a sharp increase in the unit-cell volume of Brg near the synthesis temperature of 2,300 K for the Ca-pyrolite and the komatiitic compositions (about 2%; Fig. 1b). The unit-cell volume increase could result from a Ca solubility increase because of the large ionic size of Ca^{2+} : 30% and 23% larger than Mg^{2+} and Fe^{2+} in the 8-coordinated site, respectively¹⁴, in the crystal structure of Brg. As we discuss later, our chemical analysis of the recovered samples for Ca-pyrolite and komatiitic compositions shows a significant amount of Ca in Brg, explaining the observed abrupt increase in volume. At lower pressures (about 33 GPa), the unit-cell volume of Brg did not increase with synthesis temperature in the komatiitic composition, consistent with the XRD observations of two separate perovskite phases (that is, limited Ca solubility in Brg). A similar increase in the unit-cell volume of Brg was found at the synthesis temperature of about 1,900 K in the Ca10Fe10 composition. In addition, Ca-rich Brg synthesized at higher temperatures has a SiO_6 octahedral tilting angle that is smaller by more than 7% compared with Brg synthesized at lower temperatures (Extended Data Fig. 3). This observation is also consistent with Ca incorporation in the dodecahedral site of Brg, which would reduce the tilting angle of the SiO_6 octahedra in the crystal structure of Brg (therefore less orthorhombic distortion; Methods). The increase in the unit-cell volume and the decrease in the octahedral tilting angle agree well with theoretical calculations¹⁰, which predict a greater than 1.7% volume increase and a greater than 16% octahedral tilting angle decrease for $(\text{Ca}_{0.1}\text{Mg}_{0.9})\text{SiO}_3$ Brg compared with those of MgSiO_3 Brg at 0–100 GPa.

The trends in both XRD phase identification and unit-cell volume comparison in this study remain similar at pressures between 40 GPa and 110 GPa, suggesting that the Ca solubility increase in Brg is essentially temperature driven without much sensitivity to pressure. We note that the formation of the single perovskite found here was not caused by slow kinetics because it forms at higher temperatures where kinetic effects are expected to be small.

with blue and red for the two-perovskite and the single-perovskite domains, respectively. **b**, Change in the unit-cell volumes (ΔV) of Brg as a function of synthesis temperature. The unit-cell volumes of Brg were measured upon temperature quench (300 K) at high pressures and then compared with those expected for Brg observed with CaPv for the corresponding compositions (see Methods for detail). A steep increase in the Brg volume at about 2,300 K indicates a significant increase in the Ca solubility. The black lines connect the Ca10Fe10 data at about 40 GPa, Ca-pyrolite data at about 100 GPa or komatiitic composition data at about 33 GPa, respectively. The shades are a guide for the eye. The error bars are the estimated 1σ uncertainties.

Above 2,700 K near the solidus, few data points show Ca-rich Brg existing together with a small amount of CaPv in XRD patterns (half-filled symbols in Fig. 1a). At solidus temperatures, a small amount of melt is produced, which can migrate to lower-temperature regions along both the axial and the radial directions (or along and vertical to the X-ray beam directions) because of the thermal gradients in the LHDAC. We predict that the partial melt could be rich in Ca and that the fractional crystallization of the melt at the low-temperature regions resulted in the observation of CaPv in those runs (Methods).

The STEM images and chemical maps of the recovered samples showed a substantial amount of Ca in Brg synthesized at about 2,300 K and above 60 GPa. For Ca-pyrolite, Ca-rich Brg exists as a matrix surrounding Fp grains in the sample from a run at 64 GPa and $2,300 \pm 250$ K (82 vol% for Ca-rich Brg and 18 vol% for Fp; Fig. 2c and Table 1). Quantitative analysis for the Ca-rich Brg matrix was difficult because of insufficient separation between Fp grains. Therefore, we obtained the chemical composition of Ca-rich Brg by subtracting the measured composition of Fp from that of the whole area of the map based on the estimated phase proportions (Methods). The calculation yielded 0.08 Ca atoms per formula unit (p.f.u.) for Ca-rich Brg (Table 1).

For the komatiitic composition, a sample synthesized at 100 GPa and $2,300 \pm 100$ K showed a large amount of Ca in the Ca-rich Brg matrix (0.19 Ca p.f.u.) together with magnesium (Mg), Fe and Al (Fig. 2d and Table 1). Although most of the area is Ca-rich Brg (95 vol%; Table 1), aluminium oxide (Al_2O_3) and silicon dioxide (SiO_2) were observed as minor phases, consistent with the XRD observations (Methods). The Al content in Ca-rich Brg is measured to be smaller than that in Brg synthesized at 33 GPa (0.15 Al p.f.u. and 0.20 Al p.f.u., respectively; Table 1), which explains the observed Al_2O_3 phase at the higher pressures. Another komatiitic sample synthesized at 62 GPa and $2,350 \pm 350$ K showed the same results (Extended Data Fig. 4). In contrast, a komatiitic sample

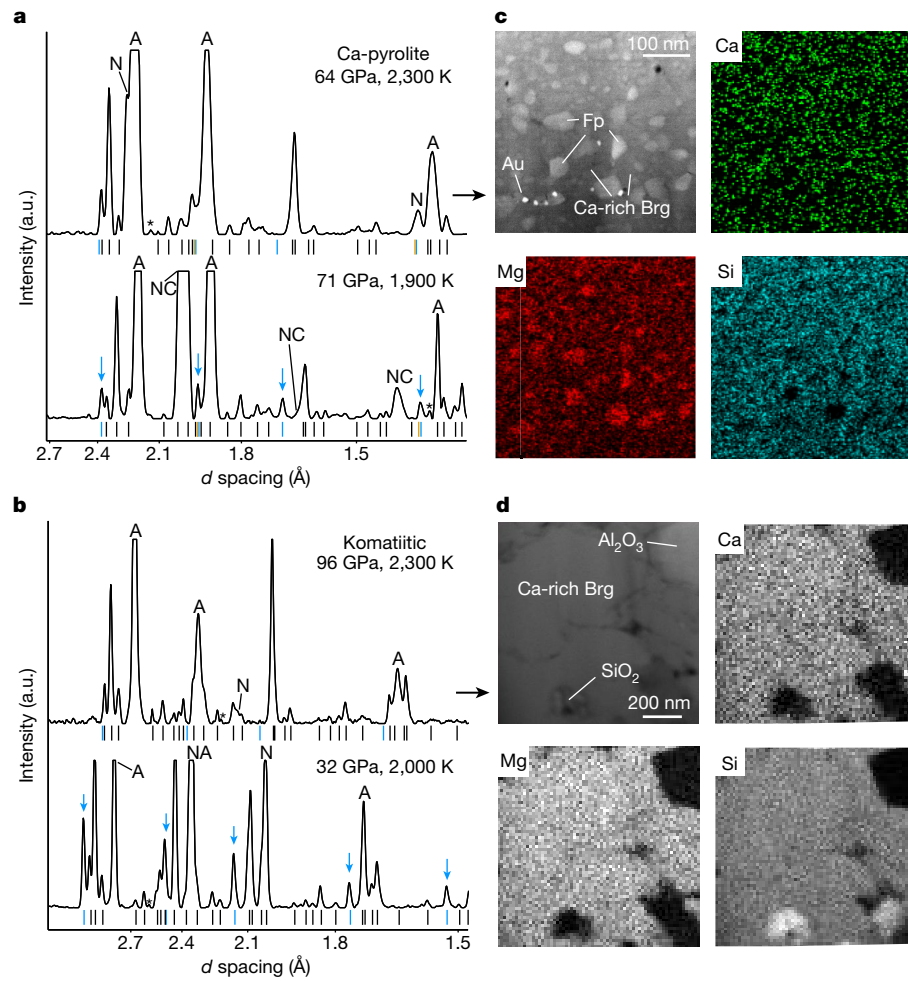


Fig. 2 | In situ XRD and ex situ electron microscopy analysis of Ca-pyrolite and the komatiitic compositions. **a,b,** The bars indicate the diffraction peak positions of bridgmanite (Brg; black), ferropericlase (Fp; orange) and CaSiO_3 perovskite (CaPv; cyan). The observed CaPv peaks are highlighted by the cyan arrows. Unidentified peaks are marked with an asterisk. Au (labelled as A) was used for pressure measurements. Ne (labelled as N) or NaCl (labelled as NC) was

used as a pressure medium. X-ray energies were 0.4133 keV (**a**) and 0.3344 keV (**b**). The background is subtracted. **c,d,** High-angle angular dark-field images (top left) and chemical maps of the recovered samples of Ca-pyrolite (**c**) and komatiitic (**d**) composition, respectively. The chemical compositions of the phases are presented in Table 1.

synthesized at the lower $P-T$ (33 GPa and $2,200 \pm 200$ K) showed separate Brg and CaPv phases (81 vol% and 15 vol%; Table 1), consistent with the XRD patterns (Fig. 2b). Point measurements revealed that Brg synthesized at 33 GPa contains a much smaller amount of Ca (0.05 p.f.u.; Table 1) than those synthesized at 62 GPa and 100 GPa, which incorporated all Ca from the starting material (0.17–0.19 Ca p.f.u.).

Compositional effects on Ca solubility

We constructed a provisional perovskite solvus diagram of the $(\text{Mg},\text{Fe})(\text{Al},\text{Si})\text{O}_3-\text{CaSiO}_3$ system (Fig. 3a). As composition data are available for a limited number of samples, we complement the dataset with the Ca content estimated from the unit-cell volume of Brg (see Methods for detail). Our Ca10Fe10 data reveal that Fe may play an important role in the Ca solubility in Brg. In this composition, a complete dissolution of Ca (0.10 p.f.u.) in Brg occurs at about 2,500 K (Fig. 1a), which is about 500 K lower than the temperature predicted for pure MgSiO_3 Brg to incorporate the same amount of Ca (0.10 p.f.u.) at the same pressure in a theoretical study¹² (Fig. 3a). The valence and spin states of Fe could be important factors¹⁵, but our data do not show clear dependence (Methods, Extended Data Table 2 and Extended Data Figs. 5 and 6). Al could also affect the Ca solubility in Brg. Although Brg in the komatiitic composition contains a larger amount of Fe (0.19–0.20 p.f.u.;

Table 1) than Brg in the Ca10Fe10 composition does (0.10 p.f.u.), the sudden increase in the unit-cell volume of Brg, and therefore the Ca solubility, occurs at a higher temperature in the komatiitic composition than in the Ca10Fe10 composition (about 2,300 K and about 1,900 K; Fig. 1b). As the komatiitic composition contains a substantial amount of Al in Brg (0.15 Al p.f.u. for Ca-rich Brg; Table 1), Al may reduce the effects of Fe on the Ca solubility, consistent with the previous prediction¹². Although the difference is within uncertainty, the steep increase in the unit-cell volume of Brg appears at a slightly higher temperature by about 50 K for Ca-pyrolite than for the komatiitic composition (Fig. 1b). The difference could be explained by the lower Fe/Al ratio in Ca-pyrolite (Table 1). From the observations above, we conjecture that mid-ocean-ridge basalt (MORB) would have separate Brg and CaPv in the lower mantle even at sufficiently high temperatures because of a factor of three more Al (that is, lower Fe/Al ratio) in the composition compared with pyrolite, which is consistent with the existing experimental results^{7,16} (Methods).

Mineralogy changes in the lower mantle

The mineralogy has long been assumed to be constant throughout the lower mantle¹ except for the bottom 400-km depths where post-perovskite can appear in the cold regions¹⁷. Our study shows that

Table 1 | Chemical compositions of the recovered samples of the komatiitic composition and Ca-pyrolite

Komatiitic composition										Pyrolite from ref. ³			Ca-pyrolite	
K33 (33 GPa, 2,200 K)			K62 (62 GPa, 2,350 K)			K100 (100 GPa, 2,300 K)				(47 GPa, 2,073 K)			CP64 (64 GPa, 2,284 K)	
Brg	CaPv	SiO ₂	Ca-rich Brg	SiO ₂	Al ₂ O ₃ ^a	Ca-rich Brg	SiO ₂	Al ₂ O ₃	Brg	Fp	CaPv ^a	Ca-rich Brg	Fp	
Si	0.83(4)	0.92(4)	0.95(2)	0.90(6)	1.00	—	0.86(3)	1.00	0.00	0.92(1)	0.01(0)	—	0.84(4)	0.00
Al	0.20(2)	0.03(2)	0.01(0)	0.15(2)	0.00	—	0.15(1)	0.00	2.00	0.09(1)	0.01(0)	—	0.13(2)	0.00
Fe	0.20(2)	0.07(3)	0.01(0)	0.19(2)	0.00	—	0.20(1)	0.00	0.00	0.08(0)	0.14(0)	—	0.08(2)	0.11(2)
Mg	0.72(4)	0.10(4)	0.02(1)	0.59(6)	0.00	—	0.60(3)	0.00	0.00	0.90(1)	0.84(1)	—	0.87(4)	0.89(4)
Ca	0.05(1)	0.88(5)	0.01(0)	0.17(2)	0.00	—	0.19(1)	0.00	0.00	0.01(0)	0.00(0)	—	0.08(2)	0.00
Vol%	81.2	14.7	4.1	>99	<1	<1	94.7	2.2	3.1	75.1	17.2	7.7	82.8	17.2
$V_{m,0}$ (cm ³ mol ⁻¹)	25.05(3)						25.50(11)			24.68(6) ^b			25.11(14)	
$V_{uc,0}$ (Å ³)	166.3(2)						169.3(7)			163.9(4) ^b			166.8(9)	
K_0 (GPa)	249(4)						245(7)			246(5) ^b			245(12)	

The total was normalized to a chemical formula for each phase. The Vinet EOS parameters at 1 bar and 300 K (molar volume, $V_{m,0}$; unit-cell volume, $V_{uc,0}$; and bulk modulus, K_0) are provided for Brg and Ca-rich Brg. Pressure derivative of bulk modulus (K'_0) was fixed as 4 for all the fits. Brg, Fp and CaPv reported in pyrolite in ref.³ are shown for comparison. ^aPoint analysis was not possible owing to very small grain size. ^b V_0 and K_0 are from Brg of Ca-pyrolite in this study (CP77). The numbers in parentheses represent uncertainty.

in the mid-mantle where temperature becomes sufficiently high (over about 2,300 K for pyrolitic composition; Fig. 3a) the Ca solubility in Brg increases steeply, leading to a change in mineralogy from Brg + CaPv (the two-perovskite domain, TPD) at shallower depths to Ca-rich Brg

(the single-perovskite domain, SPD) at greater depths. Given a gradual increase in temperature in the lower mantle, the TPD-to-SPD change would occur over a depth interval. For instance, a 50-K increase in the mid-mantle would make the depth interval for the TPD-to-SPD transition

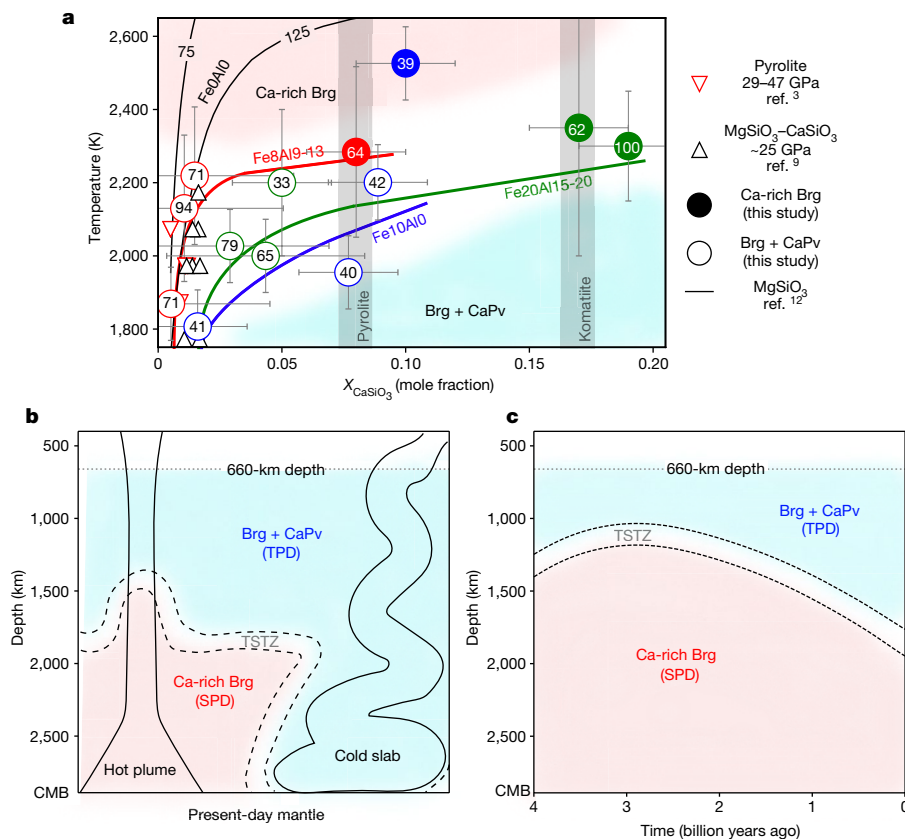


Fig. 3 | A steep increase in the solubility of CaSiO₃ in bridgmanite and mineralogical models for the lower mantle. a, Provisional perovskite solvus diagram of (Mg,Fe)(Al,Si)O₃–CaSiO₃ in the lower mantle. The open and the closed symbols denote Brg + CaPv and Ca-rich Brg (the numbers indicate the pressure in GPa), respectively. The black, red, green and blue symbols represent the pure MgSiO₃, pyrolitic, komatiitic and Ca10Fe10 compositions, respectively. Fe and Al cations per formula unit are indicated for each composition. The grey shades represent the expected amount of CaSiO₃ in pyrolitic and komatiitic

compositions, respectively. The solid lines represent provisional solvi. The error bars are the estimated 1σ uncertainties. b, A schematic diagram of the TPD and the SPD in the present-day lower mantle. The depth of the TSTZ can be modulated by lateral variations in temperature. c, Changes in the depth of the TSTZ (about 2,300 K) as a function of time in the lower mantle. The boundary depth was calculated from the mantle geotherm models^{4,5} for a Urey ratio of 0.38 (ref.²⁵) combined with our experimental results. b, c, CMB, core–mantle boundary.

Article

zone (TSTZ) 130–200 km depending on the mantle geotherm^{4,5}. At the moment, it is difficult to determine the exact depth for the TSTZ because of the uncertainties in the mantle geotherm: a higher-temperature mantle geotherm in ref. ⁵ yields about 1,500 km, whereas it is about 2,200 km for a lower-temperature mantle geotherm in ref. ⁴.

The temperature-dependent variations in the TSTZ depths can also affect our understanding on lateral heterogeneities in the lower mantle¹⁸. For example, the hot mantle plumes and the cold subducting slabs can modulate the depths of the TSTZ substantially up to ± 500 km for a variation of ± 150 K. Such behaviours of the TSTZ make it distinct from the phase transition boundary of ringwoodite to Brg + Fp at 660-km discontinuity¹⁹ and the post-perovskite boundary at D'' layer¹⁷, which are localized at narrow depth intervals.

We calculated the bulk sound speeds of Ca-rich Brg and Brg + CaPv at pressures of the lower mantle from their bulk moduli and densities obtained from the komatiitic composition at 300 K. Although uncertainties are involved, the density of Ca-rich Brg is $0.6 \pm 0.5\%$ greater than that of Brg + CaPv and the bulk modulus of Ca-rich Brg is nearly the same as that of Brg + CaPv ($\pm 1\%$) in the mid-mantle depths (Extended Data Fig. 7). Therefore, bulk sound velocity is somewhat lower (about $0.3 \pm 0.6\%$) for Ca-rich Brg (Extended Data Fig. 7). If Ca dissolution does not change the thermal parameters substantially, the changes in density and bulk sound speed could be small at the TSTZ. Although the effects of Ca dissolution on the shear velocity of Brg is yet to be measured, we infer that the TSTZ would not cause a seismic discontinuity because the change in the properties of Brg would be gradual in the TSTZ, which could span over a few hundred kilometres.

The mineralogy change proposed in this study sheds light on the ongoing controversy^{2,20,21} on whether the mantle would be chemically homogeneous with a pyrolytic composition. A recent elasticity measurement²⁰ showed that a high $\text{Fe}^{3+}/\Sigma\text{Fe}$ ratio of Brg (0.66) in pyrolyte can explain seismic properties (preliminary reference Earth model, PREM²²) in the shallow lower mantle, but their model showed a discrepancy between pyrolyte and PREM in the lower mantle below about 1,200-km depth. Another elasticity measurement²¹ argued for a larger fraction of Brg (90 vol%) than what is expected for pyrolyte (75 vol% (ref. ³)) to explain the seismic properties of the lower mantle, suggesting the Si-enriched composition compared with pyrolyte. However, if all Ca dissolves into Brg in the deep lower mantle as suggested in the present study, the effects of Ca on the seismic properties of Brg should be taken into account in such models for possible depth-dependent changes of composition in the lower mantle.

Many studies have pondered the role of Earth's deep mantle for important global events in Earth's history, such as the Great Oxidation Event²³ and the initiation of plate tectonics²⁴. The temperature-driven change from a TPD to a SPD predicts mineralogical evolution of the deep mantle even if the bulk chemical composition has been constant. In the past, the mantle should have been warmer than the present day, although details of the cooling history of the mantle remain controversial^{25–27}. The thickness of the SPD with Ca-rich Brg would have been greater in the past and becomes thinner as the mantle cools over time (Fig. 3c and Extended Data Fig. 8). Therefore, the properties of Ca-rich Brg would be essential for understanding the time-dependent changes in the lower mantle.

Online content

Any methods, additional references, Nature Research reporting summaries, source data, extended data, supplementary information, acknowledgements, peer review information; details of author contributions

and competing interests; and statements of data and code availability are available at <https://doi.org/10.1038/s41586-022-05237-4>.

1. Kesson, S., Gerald, J. F. & Shelley, J. Mineralogy and dynamics of a pyrolyte lower mantle. *Nature* **393**, 252–255 (1998).
2. Ricolleau, A. et al. Density profile of pyrolyte under the lower mantle conditions. *Geophys. Res. Lett.* **36**, L06302 (2009).
3. Irfune, T. et al. Iron partitioning and density changes of pyrolyte in Earth's lower mantle. *Science* **327**, 193–195 (2010).
4. Brown, J. & Shankland, T. Thermodynamic parameters in the Earth as determined from seismic profiles. *Geophys. J. Int.* **66**, 579–596 (1981).
5. Katsura, T., Yoneda, A., Yamazaki, D., Yoshino, T. & Ito, E. Adiabatic temperature profile in the mantle. *Phys. Earth Planet. Interiors* **183**, 212–218 (2010).
6. Lee, K. K. et al. Equations of state of the high-pressure phases of a natural peridotite and implications for the Earth's lower mantle. *Earth Planet. Sci. Lett.* **223**, 381–393 (2004).
7. Ono, S., Ohishi, Y., Isshiki, M. & Watanuki, T. In situ X-ray observations of phase assemblages in peridotite and basalt compositions at lower mantle conditions: implications for density of subducted oceanic plate. *J. Geophys. Res. Solid Earth* **110**, B02208 (2005).
8. Shimyo, R. & Hirose, K. Iron partitioning in pyrolytic lower mantle. *Phys. Chem. Miner.* **40**, 107–113 (2013).
9. Irfune, T. et al. High-pressure phase transformation in $\text{CaMgSi}_2\text{O}_6$ and implications for origin of ultra-deep diamond inclusions. *Geophys. Res. Lett.* **27**, 3541–3544 (2000).
10. Vitos, L. et al. Phase transformations between garnet and perovskite phases in the Earth's mantle: a theoretical study. *Phys. Earth Planet. Interiors* **156**, 108–116 (2006).
11. Jung, D. Y. & Schmidt, M. W. Solid solution behaviour of CaSiO_3 and MgSiO_3 perovskites. *Phys. Chem. Miner.* **38**, 311–319 (2011).
12. Muir, J. M., Thomson, A. R. & Zhang, F. The miscibility of calcium silicate perovskite and bridgemanite: a single perovskite solid solution in hot, iron-rich regions. *Earth Planet. Sci. Lett.* **566**, 116973 (2021).
13. McDonough, W. F. & Sun, S.-S. The composition of the Earth. *Chem. Geol.* **120**, 223–253 (1995).
14. Shannon, R. D. Revised effective ionic radii and systematic studies of interatomic distances in halides and chalcogenides. *Acta Crystallogr. A* **32**, 751–767 (1976).
15. Badro, J. et al. Electronic transitions in perovskite: possible nonconvecting layers in the lower mantle. *Science* **305**, 383–386 (2004).
16. Ricolleau, A. et al. Phase relations and equation of state of a natural MORB: implications for the density profile of subducted oceanic crust in the Earth's lower mantle. *J. Geophys. Res. Solid Earth* **115**, B08202 (2010).
17. Murakami, M., Hirose, K., Kawamura, K., Sata, N. & Ohishi, Y. Post-perovskite phase transition in MgSiO_3 . *Science* **304**, 855–858 (2004).
18. Lekic, V., Cottaar, S., Dziewonski, A. & Romanowicz, B. Cluster analysis of global lower mantle tomography: a new class of structure and implications for chemical heterogeneity. *Earth Planet. Sci. Lett.* **357**, 68–77 (2012).
19. Shim, S.-H., Duffy, T. S. & Shen, G. The post-spinel transformation in Mg_2SiO_4 and its relation to the 660-km seismic discontinuity. *Nature* **411**, 571–574 (2001).
20. Kurnosov, A., Marquardt, H., Frost, D. J., Ballaran, T. B. & Ziberna, L. Evidence for a Fe^{3+} -rich pyrolytic lower mantle from (Al, Fe)-bearing bridgemanite elasticity data. *Nature* **543**, 543–546 (2017).
21. Mashimo, I., Murakami, M., Miyajima, N. & Petitgirard, S. Experimental evidence for silica-enriched Earth's lower mantle with ferrous iron dominant bridgemanite. *Proc. Natl. Acad. Sci. USA* **117**, 27899–27905 (2020).
22. Dziewonski, A. M. & Anderson, D. L. Preliminary reference Earth model. *Phys. Earth Planet. Interiors* **25**, 297–356 (1981).
23. Kasting, J. F. What caused the rise of atmospheric O_2 ? *Chem. Geol.* **362**, 13–25 (2013).
24. Korenaga, J. Initiation and evolution of plate tectonics on Earth: theories and observations. *Annu. Rev. Earth Planet. Sci.* **41**, 117–151 (2013).
25. Korenaga, J. Urey ratio and the structure and evolution of Earth's mantle. *Rev. Geophys.* **46**, RG2007 (2008).
26. Davies, G. F. Effect of plate bending on the Urey ratio and the thermal evolution of the mantle. *Earth Planet. Sci. Lett.* **287**, 513–518 (2009).
27. Andrault, D., Montoux, J., Le Bars, M. & Samuel, H. The deep Earth may not be cooling down. *Earth Planetary Sci. Lett.* **443**, 195–203 (2016).
28. Lobanov, S. S. et al. Blocked radiative heat transport in the hot pyrolytic lower mantle. *Earth Planet. Sci. Lett.* **537**, 116176 (2020).
29. Andrault, D. et al. Solidus and liquidus profiles of chondritic mantle: implication for melting of the Earth across its history. *Earth Planet. Sci. Lett.* **304**, 251–259 (2011).
30. Kim, T. et al. Low melting temperature of anhydrous mantle materials at the core–mantle boundary. *Geophys. Res. Lett.* **47**, e2020GL089345 (2020).

Publisher's note Springer Nature remains neutral with regard to jurisdictional claims in published maps and institutional affiliations.

Springer Nature or its licensor holds exclusive rights to this article under a publishing agreement with the author(s) or other rightsholder(s); author self-archiving of the accepted manuscript version of this article is solely governed by the terms of such publishing agreement and applicable law.

© The Author(s), under exclusive licence to Springer Nature Limited 2022

Methods

Starting materials and sample preparations

We studied four starting compositions either as a single glass or a mixture of two glassy materials (Extended Data Table 1). The glass materials were synthesized using the laser-levitation method³¹. Ca-pyrolite was prepared by mixing pyrolite¹³ glass and CaSiO₃ glass (about 7.5:1 in mol). The increased amount of Ca enhances the detectability of CaPv in XRD patterns if it forms. Ca-pyrolite was for investigating the stability of Ca-rich Brg at *P-T* conditions. Also, the unit-cell parameters of the phases in Ca-pyrolite were measured at high pressures and 300 K. The Ca10Fe10 composition (Ca_{0.1}Mg_{0.8}Fe_{0.1}SiO₃) was prepared as a single glass for investigating the stability of Ca-rich Brg at high *P-T*. We prepared the komatiitic composition^{32,33} as a single glass. This composition was also used in ref.³⁴. The komatiitic composition contains much less Mg (Mg/Si < 1) than pyrolite and does not form Fp in the lower-mantle-related conditions³⁴. The chemical compositions of Ca-pyrolite and the komatiitic composition were confirmed using an electron probe micro analyser (JEOL JXA-8530F EPMA) combined with a wavelength-dispersive X-ray spectrometer at Arizona State University (ASU) (Extended Data Table 1).

The starting materials were powdered and mixed with about 10 wt% of gold (Au) powder (a grain size of 1–3 µm), which served as a pressure standard and a laser absorber in LHDAC experiments. The mixtures were compressed to thin foils with a thickness of about 10 µm. We loaded the sample foil into a sample chamber, a pre-indented hole in a rhenium gasket, using a micro-manipulator (Microsupport Axis Pro SS) at ASU. Four spacers (about 5-µm-sized pure sample particles) were placed between the sample foil and the diamond culet surfaces for gas or liquid medium loading. We used neon (Ne), argon (Ar) or sodium chloride (NaCl) as a pressure medium that also served as a thermal insulator. Ne was loaded using the Consortium for Materials Properties Research (COMPRES)-GeoSoilEnviroCARS (GSECARS) high-pressure gas loading system³⁵ and Ar was loaded using the gas loading system at ASU. In some runs (Extended Data Table 3), NaCl powder was dried at 120 °C for 4 h and loaded into the sample chamber as insulation layers. For samples K59B and K73B, we did not use a pressure medium (Extended Data Table 3). We cold-compressed samples in the symmetric-type diamond anvil cell to target pressures before the laser heating. The diamond culet size was 150 µm, 200 µm or 400 µm depending on the targeted pressures.

In situ XRD in LHDACs

In situ XRD experiments were performed at the 13-IDD beamline of the GeoSoilEnviroConsortium (GSECARS) sector in the Advanced Photon Source (APS)³⁶. Extended Data Table 3 summarizes all the runs conducted in this study. For sample K50 only, we conducted in situ XRD experiments at high *P-T* conditions at the 16-IDB beamline of the High-Pressure Collaborative Access Team sector in APS³⁷. At the 16-IDB beamline, we also carried out XRD measurements at room temperature for sample K100 after in situ XRD experiments at high *P-T* conditions at the 13-IDD beamline. The detailed run tables for the in situ experiments are presented in Supplementary Tables 1–5.

The diffraction patterns were measured with monochromatic X-ray beams of 0.3344 Å and 0.4133 Å at 13-IDD, 0.4340 Å at 13-BMC, and 0.4066 Å at 16-IDB (Extended Data Table 3). For the in situ experiments, we focused the laser beams on both sides of the sample and aligned the laser beams coaxially with the X-ray beam by the visual observations of the X-ray fluorescence to measure the XRD patterns at the centre of the laser heating spot. Typical beam diameters for the X-ray beam and the laser beam were 5 µm and 20 µm, respectively. We fit the thermal radiation spectra measured from both sides of the sample to the Planck grey-body equation for the estimation of temperature.

We integrated the collected X-ray diffraction images to one-dimensional diffraction patterns with the calibration parameters

obtained from the lanthanum hexaboride or cerium dioxide standard in the DIOPTAS software (version 0.5)³⁸. The exposure time was 5–10 s during heating and 10–300 s at 300 K. The diffraction patterns were analysed and fitted with a pseudo-Voigt profile function to obtain the peak positions in the PeakPo software³⁹. The unit-cell parameters were fitted using the UnitCell software⁴⁰, the Peakpo software and the GSAS-II package⁴¹. We estimated pressures by combining the measured unit-cell volumes of Au with its equation of state (EOS)⁴² in the Pytheos software⁴³. Rietveld refinement using GSAS-II was conducted to obtain phase proportions together with mass-balance calculation for run K33. Temperature uncertainties were estimated from the temperature difference between two sides of the sample combined with intrinsic uncertainty from spectroradiometry of the LHDAC samples (100 K). Pressure uncertainties were assumed to be 7% of the estimated pressures at high temperatures, which includes uncertainties from thermal equations of state of Au and temperature measurements.

An area with a diameter of about 20 µm was heated for up to 8 min during each heating cycle (Supplementary Table 1). The heating spots were chosen such that they do not overlap with previously heated spots to conduct heating on unheated fresh sample. Diffraction images were measured on a Dectris Pilatus, MarCCD or Mar345 detector. Diffraction patterns showed that the glass samples transformed to crystalline phases within 2–60 s of heating. In most runs for the *P-T* stability, we first increased the laser power at a previously heated spot until a target temperature was reached, and then translated the sample position instantly such that the same laser power could be directly applied to an unheated, fresh spot. This heating method allows for a direct increase of temperature to a targeted value for examining stable phases at different temperatures without suffering from kinetic persistence of the phases formed at low temperatures in a conventional heating method where the sample temperature is gradually increased. In our experiments, the heating duration was controlled to within 8.5 min to minimize the Soret diffusion⁴⁴, which can cause chemical segregation.

In runs K59B and K73B, the laser power was increased directly to a targeted value, raising the temperature instantaneously to a targeted value. XRD patterns were collected while at high temperature (Supplementary Table 2). These runs did not include Au. Instead, static pressure was calculated using EOSs parameters of Brg and Ca-rich Brg determined in this study (Table 1) and the thermal pressure was calculated using the EOS parameters of MgSiO₃ Brg⁴⁵. Pressure uncertainties for these runs were assumed to be 10% of the estimated pressures at high temperatures, including uncertainties from thermal EOS calculations and temperature uncertainties.

EOS fitting and unit-cell volume calculations

We fit the unit-cell volumes of Ca-rich Brg and Brg in Ca-pyrolite and the komatiitic compositions at 300 K to the Vinet EOS with a fixed pressure derivative ($K_0' = 4$; Table 1 and Extended Data Fig. 2a,b). The data for Ca-rich Brg and Brg are obtained from the decompression measurements of runs CP64 and CP77 for Ca-pyrolite composition, respectively, and runs K100 and K33 for the komatiitic composition, respectively.

The volume change shown in Fig. 1b (ΔV) was obtained from the difference between the measured values for temperature-quenched samples (300 K) and the calculated values from the fitted EOSs (Table 1) for Ca-pyrolite and the komatiitic compositions. For the Ca10Fe10 composition, the difference of the measured unit-cell volumes of Brg was obtained with respect to the unit-cell volumes of (Mg_{0.91}Fe_{0.09})SiO₃ Brg calculated using EOS parameters from ref.⁴⁶.

Chemical analysis

We recovered some of the synthesized samples of Ca-pyrolite and the komatiitic compositions (CP64, K33, K48, K62 and K100) using a micro-manipulator (Extended Data Table 3). The samples were processed in the focused ion beam (FIB; FEI Nova 200 and FEI Helios) at ASU and University of Arizona (UofA), respectively. The centre part of

Article

the heated area was extracted and mounted on a copper grid (Extended Data Fig. 9). We analysed the chemical compositions of the samples in the aberration-corrected STEM (JEOL ARM200F at ASU and Hitachi HF-5000 at UofA) combined with energy-dispersive X-ray spectroscopy (EDS). Acceleration voltages of 120 keV and 200 keV were used at ASU and UofA, respectively. For the K33 sample (Extended Data Table 3), we performed point analysis with an exposure time less than 40 s depending on the beam sensitivity at a target area. The phase proportions were estimated by mass-balance calculations based on their measured compositions. For the CP64, K48, K62 and K100 samples (Extended Data Table 3), the EDS mapping was performed to obtain chemical maps. The phase proportions were obtained from the STEM analysis. The collected EDS spectra were fitted using a Python code LMFIT⁴⁷.

Determination of calcium contents in bridgmanite

In the perovskite solvus diagram shown in Fig. 3a, the Ca content data directly determined from chemical analysis are included for Ca-rich Brg data in Ca-pyrolite and the komatiitic compositions (Table 1). However, the number of data points are limited because of: (1) challenges in recovering samples synthesized in a noble gas medium; (2) metastability of the recovered mineral phases under an intense electron beam at room conditions; and (3) extreme thinning during FIB processing required for the small grain size of the phases in the LHDAC samples. To supplement the data for Ca-rich Brg data in the Ca10Fe10 composition, the Ca content data were assumed to be 0.10 Ca p.f.u. because Ca-rich Brg is the only phase observed in the runs. For data points where Brg was observed together with CaPv, the Ca contents of Brg were estimated by a linear interpolation of the unit-cell volumes of Brg measured at 300 K. In this estimation, we assumed that the Fe and Al amounts in Brg remain the same, whereas those in CaPv are negligible. Therefore, an increase in the unit-cell volume of Brg at a given pressure and 300 K depends only on the Ca content in Brg.

We obtained the difference in the measured unit-cell volume of Brg with respect to the calculated unit-cell volume of Brg (ΔV) from the EOS fitting in this study for Ca-pyrolite and komatiitic compositions (Table 1). For the Ca10Fe10 composition, we used EOS fitting data for $(\text{Mg}_{0.91}\text{Fe}_{0.09})\text{SiO}_3$ Brg in ref. ⁴⁶. Then, Ca content (Ca#) was linearly interpolated based on the volume difference (ΔV) with two reference data points with known Ca contents. The first reference data point is the calculated Brg volume from EOS fitting (V_{ref1} , $\Delta V = 0$). For the Ca content of this reference data point (Ca#_{ref1}), because Brg can still contain a small amount of Ca even at lower temperatures^{3,9}, we assumed 0.01 Ca p.f.u. for Ca-pyrolite and the Ca10Fe10 compositions and 0.05 Ca p.f.u. for the komatiitic, which was measured from Brg synthesized at lower temperature (Table 1). For the other reference data point of the Ca-rich side, Ca-rich Brg data described above were used for the volume (V_{ref2}) and Ca content (Ca#_{ref2}). On the basis of these parameters, the Ca content of Brg of interest can be estimated from: $\text{Ca\#} = (\Delta V / \Delta V_{\text{ref2}})(\text{Ca\#}_{\text{ref2}} - \text{Ca\#}_{\text{ref1}}) + \text{Ca\#}_{\text{ref1}}$, where Ca# is Ca p.f.u. in Brg and ΔV is the volume difference of Brg relative to V_{ref1} at a given pressure and ΔV_{ref2} is the volume difference of Ca-rich Brg relative to V_{ref1} at a given pressure. The uncertainties for the Ca contents were estimated considering the uncertainties from the measured Ca contents for the reference data points, those from the assumptions we made and those from the EOS parameters.

Previous studies on the lower-mantle-related compositions

The mineral assemblages for the pyrolytic and the peridotitic compositions have been investigated by numerous experiments^{2,3,6–8,28,48–59}. Although most of the studies have documented the observation of CaPv together with Brg and Fp (+ post-perovskite, pPv), there are a few notable exceptions (Extended Data Fig. 1). For example, ref. ⁶ observed the disappearance of the diffraction peaks of CaPv in the pyrolytic sample above 65 GPa after heating between 2,000 K and 2,500 K (because they provide the range only, we plot their data at 2,250 K in Extended

Data Fig. 1). Reference ⁷ observed CaPv in XRD patterns at 28 GPa and 2,050 K, and 97 GPa and 2,100 K, but could not resolve the CaPv lines in XRD patterns at 35 GPa and 2,100 K, and 58 GPa and 2,300 K. Reference ⁸ observed CaPv at 28 GPa and 1,900 K, and 82 GPa and 2,100 K, but could not observe it at 109 GPa and 2,300 K, and 114 GPa and 2,300 K. More recently, ref. ²⁸ could not identify CaPv from XRD patterns measured at 134 GPa and about 3,000 K. Although they²⁸ observed CaPv from chemical analysis on the recovered sample synthesized at 56 GPa and up to about 2,800 K, the proportion of CaPv shown in their chemical maps is only about 1.3 vol%, whereas Brg contains up to 0.06 Ca p.f.u. Indeed, the low abundance of CaO in pyrolytic composition (<4 mol%) could make detection of a small amount of CaPv challenging. Nonetheless, these studies reported mineral assemblages with both the existence and absence of CaPv from the same starting composition. Recent melting experiments also observed the absence of CaPv, suggesting a high solubility of Ca in bridgmanite up to 129 GPa (ref. ⁶⁰). The observations of the existence and absence of CaPv at different pressures and temperatures lead to a question whether the solubility of CaSiO_3 in Brg depends on P - T conditions.

In fact, the majority of the experimental data points exist at temperatures close to or below the mantle geotherm in ref. ⁴, which is lower than other estimations^{5,61} (Extended Data Fig. 1). Although the discrepancy among the data points may be due to large uncertainties in temperatures, previous studies using LHDACs typically increased the temperature gradually such that the sample material would experience temperatures first, probably forming CaPv regardless of the target temperatures. Once a separate CaSiO_3 perovskite forms at lower temperatures, it would be difficult for CaSiO_3 to dissolve into Brg because of kinetic issues (or metastable persistence of CaPv) in the LHDAC experiments. Longer heating would not be much helpful owing to severe Fe loss through Soret diffusion⁴⁴, which would reduce the solubility of Ca in Brg according to our study and a theoretical study¹².

Figure 1a shows that our data points agree well with previous studies^{7,8,28}, which reported the absence of CaPv. As discussed above, ref. ²⁸ observed CaPv as a separate phase from chemical maps, but its volume fraction is only 1.3 vol%, much smaller than what is expected for pyrolyte³ (8 vol%) and their Brg composition contains up to 2.9 wt%. Therefore, we plotted the data point from ref. ²⁸ as Ca-rich Brg + CaPv in Fig. 1a, which appears to be consistent with our data (Methods). A data point at 35 GPa and 2,100 K from ref. ⁷ appears not in line with neighbouring data points, but if its P - T uncertainties are taken into account, this data point could be consistent with the others. The data points from ref. ⁶ are not presented in Fig. 1a because of their large temperature uncertainty. Their data points are within the range between 2,000 K and 2,500 K where we identified a transition from two perovskites to a single perovskite (Ca-rich Brg). Therefore, it is feasible that some of their data points were measured above the transition temperature.

Some previous experiments proposed that a single-perovskite phase is metastable at <35 GPa and CaPv should exist^{62,63}. At 32–35 GPa, ref. ⁶² showed a formation of a single-perovskite phase at 1,873 K and 2,073 K for 5 min of heating, whereas they showed Brg and CaPv at 2,073 K for 70 min of heating. The chemical composition of their Brg showed 0.015 Ca p.f.u., 0.20 Fe p.f.u. and 0.18 Al p.f.u. The Ca content in their Brg is consistent with pyrolyte data³ at pressures of <47 GPa as illustrated in our provisional phase diagram (Fig. 3a). In fact, their starting material contains a significant amount of Ca ($\text{Ca}_{0.51}\text{Mg}_{0.30}\text{Fe}_{0.11}\text{Al}_{0.07}\text{Si}_{0.98}\text{O}_3$); thus, it is likely that their composition always forms CaPv regardless of the P - T conditions because of too much Ca in the system beyond the Ca solubility limit. The single-perovskite phase observed from shorter heating in ref. ⁶² may be indeed metastable at <35 GPa although it is possible that the Ca content in Brg increases at higher P - T conditions. Similarly, at pressures above 21 GPa, ref. ⁶³ reported that MORB composition forms a single-perovskite phase at lower temperatures of 1,273–1,373 K in most of their runs, which dissociated into Brg and CaPv at 1,473 K. The chemical composition of Brg synthesized at 24 GPa

and 1,874 K contains 0.029 Ca p.f.u., 0.44 Fe p.f.u. and 0.37 Al p.f.u. The Ca content in their Brg is twice that in Fe- and Al-free Brg⁹ possibly because of the high Fe content (Fig. 3a). Our study suggests that Fe and high temperature promote the dissolution of CaSiO₃ in Brg. However, according to our results, Al may reduce the solubility of CaSiO₃, opposite to the effect of Fe. If this is the case, we conjecture that MORB may not be able to form a single-perovskite phase even at higher *P-T* conditions because its Fe/Al decreases with pressure (Fe/Al = 0.7, Fe/Al = 0.4 and Fe/Al = 0.3 at 33 GPa, 44 GPa and 55 GPa, respectively)¹⁶, which is consistent with existing XRD observations^{7,16}.

Stability of Ca-rich bridgmanite at ambient conditions

We performed X-ray two-dimensional scans for the Ca-pyrolite and the komatiitic samples upon pressure quench at room conditions. We observed the complete disappearance of CaPv in most diffraction patterns, consistent with previous studies in which CaPv amorphized upon pressure quench to 1 bar (refs. ^{64,65}). Ca-rich Brg in both compositions and Brg in Ca-pyrolite were identified with diffraction peaks, indicating a crystalline state for the phases. Some spots show stronger intensities with sharp peaks, where the pressure was still measured to be 0–1 GPa using the EOS parameters of Au even after the diamond anvil cell was open by set screws (Supplementary Tables 3 and 4). The measured pressure up to 1 GPa could be caused by residual strain.

The measured unit-cell volumes of Ca-rich Brg and Brg at room conditions are included in the EOS fitting (Supplementary Tables 3 and 4). The fitting yielded the unit-cell volumes at ambient conditions (V_0) of 166.4(4) Å³ and 164.1(10) Å³ for Ca-rich Brg and Brg in Ca-pyrolite, respectively. For the komatiitic composition, they were 169.5(4) Å³ and 166.3(2) Å³ for Ca-rich Brg and Brg, respectively (Table 1). Also, it yielded a bulk modulus at ambient conditions (K_0) of 254(5) GPa and 242(10) GPa for Ca-rich Brg and Brg in Ca-pyrolite and 245(4) GPa and 249(4) GPa in the komatiitic composition, respectively (Table 1). For the Ca-pyrolite composition, the existence of Fp was clearly identified at ambient conditions with relatively larger peak intensities owing to the reduced peak intensity of Brg that overlapped with the Fp diffraction lines at higher pressures. This observation is consistent with the previous report of diminishing diffraction intensities of Fe, Al-bearing Brg at ambient conditions⁶⁶.

Effects of the Ca dissolution on the unit-cell parameters of bridgmanite

We compared the molar volume of Ca-rich Brg with the combined volume of Brg + CaPv assemblage at 300 K and 0–100 GPa. The volumes of the individual phases were obtained from their EOSs. The molar volume of the Brg + CaPv assemblage was calculated using the expected molar ratio of the phases from the starting composition (8:2; Extended Data Table 1) for Ca-pyrolite, assuming that all the CaSiO₃ component forms pure CaSiO₃ perovskite (Extended Data Fig. 3a). The molar volume of CaPv was calculated using the EOS parameters from ref. ⁶⁴. For the komatiitic composition, the molar ratio of Brg and CaPv was obtained from the phase proportions of Brg and CaPv at 33 GPa where two separate perovskite phases were observed (86:14; Extended Data Fig. 3b). Then we assumed the phase proportions of Brg and CaPv remain the same at 0–100 GPa. The volume of Ca-rich Brg is marginally smaller by <1.1 ± 0.6% for Ca-pyrolite or greater by <0.3 ± 0.3% for the komatiitic composition than that of the Brg + CaPv assemblage up to 100 GPa, which are within the uncertainties of the estimations (Fig. 2a,b). Combined with the measured compositions of the komatiitic composition, we also found that Ca-rich Brg is slightly denser by <0.6 ± 0.8% than the Brg + CaPv assemblage up to 100 GPa at 300 K, also within the uncertainties.

We found that the orthorhombic distortion of Brg decreases when a substantial amount of Ca dissolves in its crystal structure. We compared the unit-cell parameters of Ca-rich Brg and Brg at the same pressures and 300 K. For Ca-pyrolite, both the *a* and *c* parameters are larger in

Ca-rich Brg than in Brg. The difference in the *a* parameter between Ca-rich Brg and Brg is greater than the difference in the *c* parameter, resulting in the smaller *c/a* ratio in Ca-rich Brg. The *b* parameter seems similar between Ca-rich Brg and Brg, therefore the smaller *b/a* ratio in Ca-rich Brg. For the komatiitic composition, the *a*, *b* and *c* parameters are all larger in Ca-rich Brg than in Brg. However, the difference in the *a* parameter between Ca-rich Brg and Brg is the largest among the unit-cell parameters. Therefore, both the *c/a* ratio and the *b/a* ratio are smaller in Ca-rich Brg than in Brg, consistent with those found in Ca-pyrolite. These changes result in the smaller tilting angle of the SiO₆ octahedra of Ca-rich Brg (that is, less distortion of the dodecahedral A site). The octahedral tilting angle can be a measure of the anisotropy of the orthorhombic perovskite with respect to the ideal cubic perovskite ($\varphi = 0^\circ$)⁶⁷. Extended Data Fig. 3c,d shows the octahedral tilting angle data and the fitted lines. The octahedral tilting angle of Ca-rich Brg is smaller by at least 7% than that of Brg in Ca-pyrolite and the komatiitic compositions at 300 K.

Previous studies have shown that the octahedral tilting angle of Brg is increased by Al (ref. ⁶⁸) and Fe³⁺ (ref. ⁶⁹), whereas it is decreased by Fe²⁺ (ref. ⁴⁶). For example, in the komatiitic composition, the Al amount is smaller in Ca-rich Brg than in Brg (0.15 p.f.u. and 0.20 p.f.u., respectively; Table 1) because some amount of Al exists in a separate Al₂O₃ phase besides Ca-rich Brg. Reference ⁶⁸ reported that 0.5 Al p.f.u. increases the octahedral tilting angle of Brg by about 2°, relative to MgSiO₃ Brg at 0–100 GPa. Thus, the effect resulting from the difference of 0.05 Al p.f.u. between Ca-rich Brg and Brg in the komatiitic composition would be significantly smaller. In addition, synchrotron Mössbauer spectroscopy (SMS) measurements showed that Fe^{3+}/ΣFe is only 10% larger in Ca-rich Brg of CF58M than in Brg of CF59M (55.5% and 45.5%, respectively; Extended Data Fig. 6 and Extended Data Table 2). If Fe^{3+}/ΣFe in Ca-rich Brg and Brg in the komatiitic composition are similar to the measured values in the Ca30Fe13 composition (Ca_{0.3}Mg_{0.64}Fe_{0.13}Si_{0.94}O₃), the effects of Fe³⁺ and Fe²⁺ on the octahedral tilting angle would be similar between Ca-rich Brg and Brg. If this is the case, the large difference of the octahedral tilting angle (about 2.6°, at 0–100 GPa; Extended Data Fig. 3d) between Ca-rich Brg and Brg in the komatiitic composition should be caused mainly by Ca in the dodecahedral site.}}

The effects of Ca on the Brg structure appear to be similar to those of Fe²⁺. The substitution of Fe²⁺ for Mg not only expands the unit-cell volume of Brg⁷⁰ but also decreases the octahedral tilting angle of Brg⁴⁵. The octahedral tilting angle of (Mg,Fe)SiO₃ Brg increases with increasing pressure by about 0.05° per GPa (ref. ⁴⁵), similar to 0.05° per GPa of Ca-rich Brg in Ca-pyrolite, but larger than 0.03° per GPa of Ca-rich Brg in the komatiitic composition (Extended Data Fig. 3c). The similar effects on the unit-cell parameters of Brg between Ca and Fe²⁺ are likely because of their larger ionic sizes than Mg in the A site of the Brg structure. However, the size difference from Mg is much greater for Ca than for Fe²⁺ (1.13 Å, 0.92 Å and 0.86 Å for Ca²⁺, Fe²⁺ and Mg²⁺ in the 12-coordinated site, respectively)¹⁴. Therefore, the effects of Ca on the crystal structure of Brg may be greater than those of Fe²⁺ if their amounts are equal in Brg. In the pyrolytic composition, Brg would contain 0.04–0.06 Fe²⁺ p.f.u. (ref. ³), in the lower mantle, which is sufficient to alter the distortion in the crystal structure of Brg⁷¹. Compared with Fe, the similar or slightly greater amount of Ca may exist in Ca-rich Brg in the pyrolytic composition (about 0.06 Ca p.f.u.). Therefore, the effects of Ca dissolution in Brg in the lower mantle could be larger than those of Fe²⁺ in terms of the crystal structure of Brg.

Mineral assemblage of Ca-rich bridgmanite and CaSiO₃ perovskite found in some runs

From some of the data points at very high temperatures, >2,700 K (Fig. 1a), we observed separate CaPv at 55–100 GPa. The unit-cell parameters of Brg in these runs are consistent with those of Ca-rich Brg at high pressures and 300 K (expanded volume and reduced tilting

Article

of the SiO_6 octahedra), which suggests that a significant amount of Ca still exists in Brg (therefore Ca-rich Brg) (Supplementary Table 3). The peak temperatures during heating for these runs might have reached the solidus where partial melt is generated. The amount of melt may be small because we did not observe diffuse scattering of melt in the in situ XRD patterns. The partial melt might have migrated to colder regions from the centre of the hotspot and crystallized CaPv because partial melt may contain more Ca. This predicted process may explain the observation of separate CaPv in these high-temperature runs. Such migration of elements along thermal gradients can occur even in a very short period of heating (<5 s) if the temperature is sufficiently high near the solidus⁷². These data points are indeed close to the reported solidus temperatures of chondritic²⁹ and pyrolytic composition³⁰ as shown in Fig. 1a. There is an exception at 100 GPa and 2,900 K below the solidus, which occurred possibly because of the larger temperature uncertainties than what we estimated.

In addition, two data points at 75 GPa and about 2,300 K also showed separate CaPv together with Ca-rich Brg, which are adjacent to the boundary shown in Fig. 1a. The expanded volume and reduced tilting of the SiO_6 octahedra confirmed the existence of Ca-rich Brg (Supplementary Tables 2 and 5). The peak intensities of CaPv in these runs are significantly lower than those found in the other runs that formed Ca-rich Brg only, suggesting that a substantial amount of Ca still dissolved in Brg, whereas some amount of Ca formed CaPv. As discussed in the main text, the solubility of Ca in Brg may gradually increase with increasing temperature across about 2,300 K. During the gradual solubility increase, separate CaPv could still remain in the system but in a smaller amount.

Ca-rich bridgmanite in Ca-pyrolite

The XRD patterns of Ca-pyrolite showed Brg as the dominant phase at the explored P - T conditions (Extended Data Fig. 2b). Fp was also identified by its 200 and 220 lines, but difficult to resolve in some runs owing to an overlap with the intense diffraction peaks of Brg (Extended Data Fig. 2b). In the STEM analysis, the Brg matrix surrounds the Fp grains (a few tens of nanometres in diameter) with phase proportions of 82 vol% and 18 vol% (Table 1). The calculated Ca amount for Brg is 0.08 p.f.u. (Table 1), smaller than what is expected for the starting composition. As this starting material is a mechanical mixture of pyrolite glass and CaSiO_3 glass, some degree of inhomogeneity in Ca content may exist. This may explain the data scatter in the EOS fit for Ca-rich Brg shown in Extended Data Fig. 3a (red open circles).

Ca-rich bridgmanite in the komatiitic composition

We synthesized four samples from the komatiitic starting composition at 33 GPa, 48 GPa, 62 GPa and 100 GPa and at high temperatures to investigate the chemical composition and the unit-cell parameters of Brg (K33, K48, K62 and K100, respectively; Extended Data Table 3). The synthesis temperatures were at $2,200 \pm 200$ K for K33, $2,000 \pm 200$ K for K48, $2,350 \pm 350$ K for K62 and $2,300 \pm 150$ K for K100. The samples were scanned with the laser beams to ensure complete crystallization of a sufficiently large area for chemical analysis.

The XRD patterns of K33 show that Brg is the dominant phase. CaPv was clearly identified with the 110, 111, 200, 211 and 220 lines (Extended Data Fig. 2a). A stishovite (Stv) 110 line was also observed with a low intensity in some runs. The STEM analysis identified Brg, CaPv and Stv (Table 1), consistent with the XRD observations. The measured chemical compositions of individual phases and mass-balance calculation with respect to the starting composition show 81.2 vol%, 14.7 vol% and 4.1 vol% for Brg, CaPv and Stv (Table 1) in the K33 sample, respectively.

Similar results were obtained for K48. The XRD patterns show robust diffraction lines of 110, 111 and 200 for CaPv as well as Brg diffraction lines (Extended Data Fig. 4b). Stv 110, 101 and 111 lines were observed with lower intensities. The chemical maps consistently show that CaPv

and Stv exist in the Brg matrix (Extended Data Fig. 4d), agreeing with the XRD patterns. Owing to the large thickness, we could not reliably determine chemical compositions of the mineral phases in this sample.

For K62, the XRD patterns show Brg as a major phase (Extended Data Fig. 4a). Stv was observed as a minor phase with the 110 and 211 lines. Some diffraction patterns of K62 also show a corundum (Crn) 104 line with a low intensity. We observed weak CaPv 110 and 200 lines (Extended Data Fig. 4a). In the STEM analysis, Brg exists as a matrix with minor Stv, Crn and a few grains of CaPv (Extended Data Fig. 4b). Brg contains 0.17 Ca p.f.u., which suggests that most of the Ca is incorporated in Brg (Ca-rich Brg). We could not conduct point analysis on CaPv and Cor owing to their small grain sizes (Extended Data Fig. 4). The phase proportions estimated from the STEM analysis showed that most of the sample is Ca-rich Brg (>99 vol%; Table 1).

For K100, two sets of XRD patterns were observed from different heating spots in terms of mineralogy (Extended Data Fig. 2a): Ca-rich Brg only (K100-1), and Ca-rich Brg + CaPv (K100-2). The XRD intensities of the CaPv peaks in K100-2 are much weaker than those in K33, which suggests that the amount of CaPv is smaller in K100-2 than in K33. As shown in Extended Data Fig. 3b, the unit-cell volumes of Ca-rich Brg in K100-2 are smaller than those of Ca-rich Brg in K100-1, but still larger than those of Brg (Extended Data Fig. 3b). Therefore, Ca-rich Brg in K100-2 contains some amount of Ca, but not as much as the amount in Ca-rich Brg of K100-1 where no CaPv was observed. The synthesis temperature for this sample was about 2,300 K, in which the steep increase in the Ca solubility occurs (Fig. 1). Thus, we interpret that the mineral assemblage of K100-2 (Ca-rich Brg + CaPv) formed at a slightly lower temperature than the temperature at which the mineral assemblage of K100-1 formed within the temperature uncertainties. In the STEM analysis, the chemical maps show a substantial amount of Ca dissolved in Brg, therefore Ca-rich Brg (0.19 Ca p.f.u.; Table 1 and Fig. 2d). In addition, they reveal Al_2O_3 and SiO_2 as minor phases, consistent with the XRD observations. The 111, 002, 211, 022, 402 or 213 lines of the Rh_2O_3 (II)-type Al_2O_3 phase were found with low intensities in the most runs, whereas the 110 or 011 lines of CaCl_2 -type SiO_2 was found with low intensities in some of the runs (Extended Data Fig. 2a). In the XRD patterns, there are a few unidentified peaks with low intensities. They were not observed consistently in different runs with different compositions and P - T conditions. They appear as a single dot in two-dimensional diffraction images.

Synchrotron Mössbauer analysis for Fe in bridgmanite

To investigate the valence and the spin states of Fe in Brg, a sample with the $\text{Ca}_{30}\text{Fe}_{13}$ composition ($\text{Ca}_{0.3}\text{Mg}_{0.65}\text{Fe}_{0.13}\text{Si}_{0.96}\text{O}_3$) was prepared by mixing $\text{Mg}_{0.9}\text{Fe}_{0.2}\text{Si}_{0.9}\text{O}_3$ glass (95% of Fe is enriched with ^{57}Fe) and CaSiO_3 glass (about 2.5:1 in mol). $\text{Fe}^{3+}/\Sigma \text{Fe}$ of the $\text{Mg}_{0.9}\text{Fe}_{0.2}\text{Si}_{0.9}\text{O}_3$ glass starting material was 53%, which was measured using Mössbauer spectroscopy at Sector 3-IDB, APS. The chemical composition of the $\text{Ca}_{30}\text{Fe}_{13}$ sample was confirmed using an electron probe microanalyser (JEOL JXA-8530F EPMA) combined with a wavelength-dispersive X-ray spectrometer at ASU (Extended Data Table 1).

We synthesized two samples of the composition at about 58 GPa and $2,400 \pm 100$ K (CF58M) and at about 59 GPa and $2,150 \pm 300$ K (CF59M; Extended Data Table 3) at ASU. Then, the XRD patterns were measured at room temperature at sector 13-BMC at APS. We observed a single phase of Brg in CF58M, whereas we observed CaPv together with Brg in CF59M (Extended Data Fig. 5). The molar volume of Brg at about 58 GPa and 300 K is larger in CF58M than in CF59M ($21.13(1)$ cm^3 and $20.93(1)$ cm^3 , respectively), suggesting that Brg in CF58M incorporated a considerable amount of Ca (Ca-rich Brg). Also, the octahedral tilting angle is smaller in Ca-rich Brg of CF58M than in Brg of CF59M ($20.59(3)^\circ$ and $21.57(2)^\circ$, respectively), consistent with what was observed in Ca-pyrolite and the komatiitic composition.

For SMS, nuclear forward scattering was conducted at sector 3-IDB of APS. A 14.4-keV X-ray beam was focused on an area of $6 \times 6 \mu\text{m}^2$ in the

sample. The storage ring was operated in top-up mode with 24 bunches separated by 153 ns. Nuclear resonant scattering was measured in a time window of 15–130 ns for an exposure time of 5–6 h. The *in situ* SMS was conducted for samples CF58M and CF59M at 58 GPa and 59 GPa, respectively, in diamond anvil cells (Extended Data Fig. 6). FeSO₄·7H₂O and stainless steel were used as standard materials for samples CF58M and CF59M, respectively. The measured spectra were fitted by using the CONUSS package⁷³.

The SMS measurements showed that Fe³⁺/ΣFe is greater by 10% in Ca-rich Brg of CF58M than in Brg of CF59M (55.5% and 45.5%, respectively; Extended Data Table 2). Compared with the starting material, Fe³⁺/ΣFe (53%) remains nearly the same in CF58M, whereas slightly reduced in CF59M. As the change of Fe³⁺/ΣFe from the starting material is not large for both samples, it is uncertain whether the difference in Fe³⁺/ΣFe between Ca-rich Brg and Brg is caused by different synthesis temperature and is related to the solubility of Ca in Brg. The quadrupole-splitting values of Fe³⁺ are similar between Ca-rich Brg and Brg (1.82 mm s⁻¹ and 1.73 mm s⁻¹, respectively; Extended Data Table 2). These quadrupole-splitting values are similar to or slightly lower than the predicted values of the low-spin Fe³⁺ in (Mg,Fe)(Fe,Si)O₃ Brg by density-functional-theory calculations (1.8–2.9 mm s⁻¹ for the B site)⁷⁴, but greater by about 0.3–0.4 mm s⁻¹ than those from previous measurements in (Mg,Fe)(Fe,Si)O₃ Brg^{75,76}. Therefore, the majority of Fe³⁺ may be low spin at about 60 GPa.

Previous studies have shown that the spin state of Fe³⁺ in Brg undergoes a transition from the high spin to the low spin^{69,74,77} at about 40–60 GPa. High-spin Fe³⁺ would substitute for Mg²⁺ in the A site, while Al³⁺ substitutes for Si⁴⁺ in the B site in Brg⁷⁴. The ionic size of Fe³⁺ becomes smaller with the spin transition (0.65 Å and 0.55 Å for the high spin and low spin, respectively, for the six-coordinated site)¹⁴, resulting in a cation exchange with Si⁴⁺ in the B site⁷⁷. Therefore, the change in the substitution mechanism driven by the spin transition of Fe³⁺ could be related to the Ca solubility increase in Brg. Further investigation is needed to understand how the valence and spin states of Fe affects the solubility of Ca in Brg.

Data availability

Datasets for this research are available online at <https://doi.org/10.5281/zenodo.6979058>.

31. Tangeman, J. A. et al. Vitreous forsterite (Mg₂SiO₄): synthesis, structure, and thermochemistry. *Geophys. Res. Lett.* **28**, 2517–2520 (2001).
32. Herzberg, C., Condie, K. & Korenaga, J. Thermal history of the Earth and its petrological expression. *Earth Planet. Sci. Lett.* **292**, 79–88 (2010).
33. Johnson, T. E., Brown, M., Kaus, B. J. & VanTongeren, J. A. Delamination and recycling of Archaean crust caused by gravitational instabilities. *Nat. Geosci.* **7**, 47–52 (2014).
34. Ko, B. et al. Mineralogy and density of Archean volcanic crust in the mantle transition zone. *Phys. Earth Planet. Interiors* **305**, 106490 (2020).
35. Rivers, M. et al. The COMPRES/GSECARS gas-loading system for diamond anvil cells at the Advanced Photon Source. *High Press. Res.* **28**, 273–292 (2008).
36. Prakapenka, V. et al. Advanced flat top laser heating system for high pressure research at GSECARS: application to the melting behavior of germanium. *High Press. Res.* **28**, 225–235 (2008).
37. Meng, Y., Hrubiak, R., Rod, E., Boehler, R. & Shen, G. New developments in laser-heated diamond anvil cell with *in situ* synchrotron X-ray diffraction at High Pressure Collaborative Access Team. *Rev. Sci. Instrum.* **86**, 072201 (2015).
38. Prescher, C. & Prakapenka, V. B. Dioplas: a program for reduction of two-dimensional X-ray diffraction data and data exploration. *High Press. Res.* **35**, 223–230 (2015).
39. Shim, S.-H. PeakPo—a python software for X-ray diffraction analysis at high pressure and high temperature. Zenodo <https://doi.org/10.5281/zenodo.842949> (2017).
40. Holland, T. & Redfern, S. UNITCELL: a nonlinear least-squares program for cell-parameter refinement and implementing regression and deletion diagnostics. *J. Appl. Crystallogr.* **30**, 84–84 (1997).
41. Toby, B. H. & Von Dreele, R. B. GSAS-II: the genesis of a modern open-source all purpose crystallography software package. *J. Appl. Crystallogr.* **46**, 544–549 (2013).
42. Dorogokupets, P. & Dewaele, A. Equations of state of MgO, Au, Pt, NaCl-B1, and NaCl-B2: internally consistent high-temperature pressure scales. *High Press. Res.* **27**, 431–446 (2007).
43. Shim, S.-H. Pytheos—a Python tool set for equations of state. Zenodo <https://doi.org/10.5281/zenodo.802392> (2017).
44. Simmyo, R. & Hirose, K. The Soret diffusion in laser-heated diamond-anvil cell. *Phys. Earth Planet. Interiors* **180**, 172–178 (2010).
45. Stamenkovic, V., Breuer, D. & Spohn, T. Thermal and transport properties of mantle rock at high pressure: applications to super-earths. *Icarus* **216**, 572–596 (2011).
46. Dorfman, S. M., Meng, Y., Prakapenka, V. B. & Duffy, T. S. Effects of Fe-enrichment on the equation of state and stability of (Mg,Fe)SiO₃ perovskite. *Earth Planet. Sci. Lett.* **361**, 249–257 (2013).
47. Newville, M. et al. LMFIT: Non-linear least-square minimization and curve-fitting for Python. *Astrophysics Source Code Library* ascl:1606.014 (2016).
48. Irfune, T., Ringwood, A. & Hibberson, W. Subduction of continental crust and terrigenous and pelagic sediments: an experimental study. *Earth Planet. Sci. Lett.* **126**, 351–368 (1994).
49. Nishiyama, N. & Yagi, T. Phase relation and mineral chemistry in pyrolite to 2200 °C under the lower mantle pressures and implications for dynamics of mantle plumes. *J. Geophys. Res. Solid Earth* **108**, 2255 (2003).
50. Nishiyama, N., Irfune, T., Inoue, T., Ando, J.-I. & Funakoshi, K.-I. Precise determination of phase relations in pyrolite across the 660 km seismic discontinuity by *in situ* X-ray diffraction and quench experiments. *Phys. Earth Planet. Interiors* **143**, 185–199 (2004).
51. Ono, S., Ohishi, Y. & Mibe, K. Phase transition of Ca-perovskite and stability of Al-bearing Mg-perovskite in the lower mantle. *Am. Mineral.* **89**, 1480–1485 (2004).
52. Murakami, M., Hirose, K., Sata, N. & Ohishi, Y. Post-perovskite phase transition and mineral chemistry in the pyrolytic lowermost mantle. *Geophys. Res. Lett.* **32**, L03304 (2005).
53. Ono, S. & Oganov, A. R. *In situ* observations of phase transition between perovskite and CaIrO₃-type phase in MgSiO₃ and pyrolytic mantle composition. *Earth Planet. Sci. Lett.* **236**, 914–932 (2005).
54. Ohta, K., Hirose, K., Lay, T., Sata, N. & Ohishi, Y. Phase transitions in pyrolite and MORB at lowermost mantle conditions: implications for a MORB-rich pile above the core–mantle boundary. *Earth Planet. Sci. Lett.* **267**, 107–117 (2008).
55. Kubo, A., Ito, E., Katsura, T., Fujino, K. & Funakoshi, K.-I. *In situ* X-ray diffraction of pyrolite to 40 GPa using Kawai-type apparatus with sintered diamond anvils: possibility for the existence of iron-rich metallic particles in the lower mantle. *High Press. Res.* **28**, 351–362 (2008).
56. Sanehira, T. et al. Density profiles of pyrolite and MORB compositions across the 660 km seismic discontinuity. *High Press. Res.* **28**, 335–349 (2008).
57. Ohta, K. et al. Electrical conductivities of pyrolytic mantle and MORB materials up to the lowermost mantle conditions. *Earth Planet. Sci. Lett.* **289**, 497–502 (2010).
58. Auzende, A.-L. et al. Synthesis of amorphous MgO-rich peridotitic starting material for laser-heated diamond anvil cell experiments—application to iron partitioning in the mantle. *High Press. Res.* **31**, 199–213 (2011).
59. Simmyo, R., Hirose, K., Muto, S., Ohishi, Y. & Yasuhara, A. The valence state and partitioning of iron in the Earth's lowermost mantle. *J. Geophys. Res. Solid Earth* **116**, B07205 (2011).
60. Nabie, F. et al. Investigating magma ocean solidification on Earth through laser-heated diamond anvil cell experiments. *Geophys. Res. Lett.* **48**, e2021GL092446 (2021).
61. Stacey, F. D. A thermal model of the Earth. *Phys. Earth Planet. Interiors* **15**, 341–348 (1977).
62. Asahara, Y. et al. Formation of metastable cubic-perovskite in high-pressure phase transformation of Ca(Mg,Fe,Al)Si₂O₆. *Am. Mineral.* **90**, 457–462 (2005).
63. Sano, A. et al. *In situ* X-ray diffraction study of the effect of water on the garnet–perovskite transformation in MORB and implications for the penetration of oceanic crust into the lower mantle. *Phys. Earth Planet. Interiors* **159**, 118–126 (2006).
64. Chen, H. et al. Crystal structure of CaSiO₃ perovskite at 28–62 GPa and 300 K under quasi-hydrostatic stress conditions. *Am. Mineral.* **103**, 462–468 (2018).
65. Shim, S.-H., Jeanloz, R. & Duffy, T. S. Tetragonal structure of CaSiO₃ perovskite above 20 GPa. *Geophys. Res. Lett.* **29**, 19–19–4 (2002).
66. Dorfman, S. M., Shieh, S. R., Meng, Y., Prakapenka, V. B. & Duffy, T. S. Synthesis and equation of state of perovskites in the (Mg,Fe)₃Al₂Si₃O₁₂ system to 177 GPa. *Earth Planet. Sci. Lett.* **357**, 194–202 (2012).
67. O'keeffe, M., Hyde, B. & Bovin, J.-O. Contribution to the crystal chemistry of orthorhombic perovskites: MgSiO₃ and NaMgF₃. *Phys. Chem. Miner.* **4**, 299–305 (1979).
68. Walter, M. et al. Phase relations and equation-of-state of aluminous Mg-silicate perovskite and implications for Earth's lower mantle. *Earth Planet. Sci. Lett.* **222**, 501–516 (2004).
69. Cataldi, K. et al. Spin state of ferric iron in MgSiO₃ perovskite and its effect on elastic properties. *Earth Planet. Sci. Lett.* **289**, 68–75 (2010).
70. Knittle, E. & Jeanloz, R. Synthesis and equation of state of (Mg,Fe)SiO₃ perovskite to over 100 gigapascals. *Science* **235**, 668–670 (1987).
71. Andraut, D., Bolfan-Casanova, N. & Guignot, N. Equation of state of lower mantle (Al,Fe)-MgSiO₃ perovskite. *Earth Planet. Sci. Lett.* **193**, 501–508 (2001).
72. Nomura, R. et al. Spin crossover and iron-rich silicate melt in the Earth's deep mantle. *Nature* **473**, 199–202 (2011).
73. Sturhahn, W. CONUSS and PHOENIX: evaluation of nuclear resonant scattering data. *Hyperfine Interact.* **125**, 149–172 (2000).
74. Hsu, H., Blaha, P., Cococcioni, M. & Wentzcovitch, R. M. Spin-state crossover and hyperfine interactions of ferric iron in MgSiO₃ perovskite. *Phys. Rev. Lett.* **106**, 118501 (2011).
75. Simmyo, R., McCammon, C. & Dubrovinsky, L. The spin state of Fe³⁺ in lower mantle bridgmanite. *Am. Mineral.* **92**, 1263–1269 (2017).
76. Liu, J. et al. Valence and spin states of iron are invisible in Earth's lower mantle. *Nat. Commun.* **9**, 1284 (2018).
77. Fujino, K. et al. Spin transition of ferric iron in Al-bearing Mg-perovskite up to 200 GPa and its implication for the lower mantle. *Earth Planet. Sci. Lett.* **317**, 407–412 (2012).

Acknowledgements K. Mossman and M. R. Gutierrez assisted with the FIB and STEM measurements at Arizona State University; and Y.-J. Chang assisted with the FIB and STEM measurements at University of Arizona. This work was supported by National Science Foundation (EAR-1725094). This research used resources of the Advanced Photon Source (APS), a US Department of Energy (DOE) Office of Science User Facility operated for the DOE Office of Science by Argonne National Laboratory under contract number DE-AC02-06CH11357. We acknowledge the support of GeoSoilEnviroCARS (Sector 13), which is supported by the National Science Foundation (NSF) - Earth Sciences (EAR-1634415), and the Department of Energy, Geosciences (DE-FG02-94ER14466). Use of the COMPRES-GSECARS

Article

gas loading system was also supported by COMPRES under NSF Cooperative Agreement EAR - 1606856. High-Pressure Collaborative Access Team (Sector 16) is supported by DOE-NNSA Grant DE-NA0001974 and DOE-BES Grant DE-FG02-99ER45775.

Author contributions B.K. conceptualized the project, designed and performed the experiments, analysed data and wrote the manuscript. S.-H.S. conceptualized and supervised the project, acquired funding, designed experiments and wrote the manuscript. E.G., V.P., Y.M. and D.Z. provided resources for the in situ XRD measurements and supervised the experiments. E.E.A. and W.B. provided resources for the SMS measurements and supervised the experiments. All authors reviewed the manuscript.

Competing interests The authors declare no competing interests.

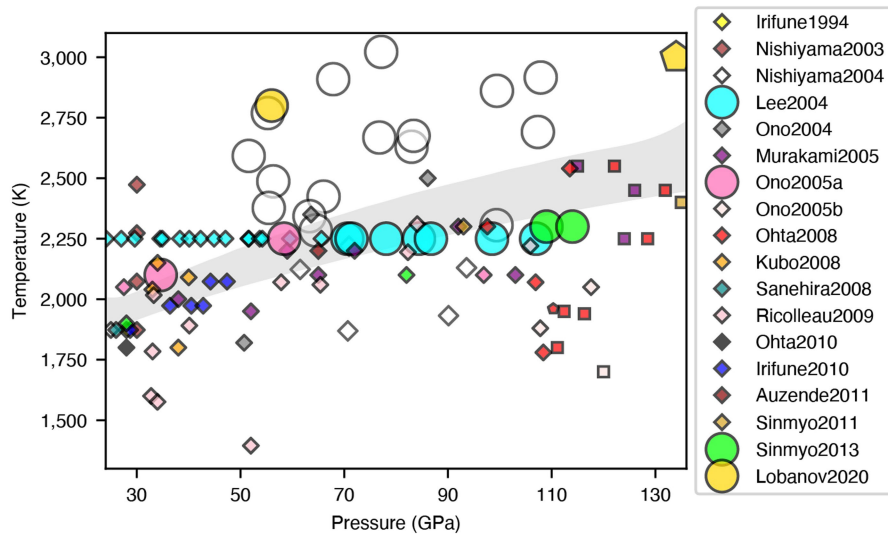
Additional information

Supplementary information The online version contains supplementary material available at <https://doi.org/10.1038/s41586-022-05237-4>.

Correspondence and requests for materials should be addressed to Byeongkwan Ko or Sang-Heon Shim.

Peer review information *Nature* thanks the anonymous reviewers for their contribution to the peer review of this work. Peer reviewer reports are available.

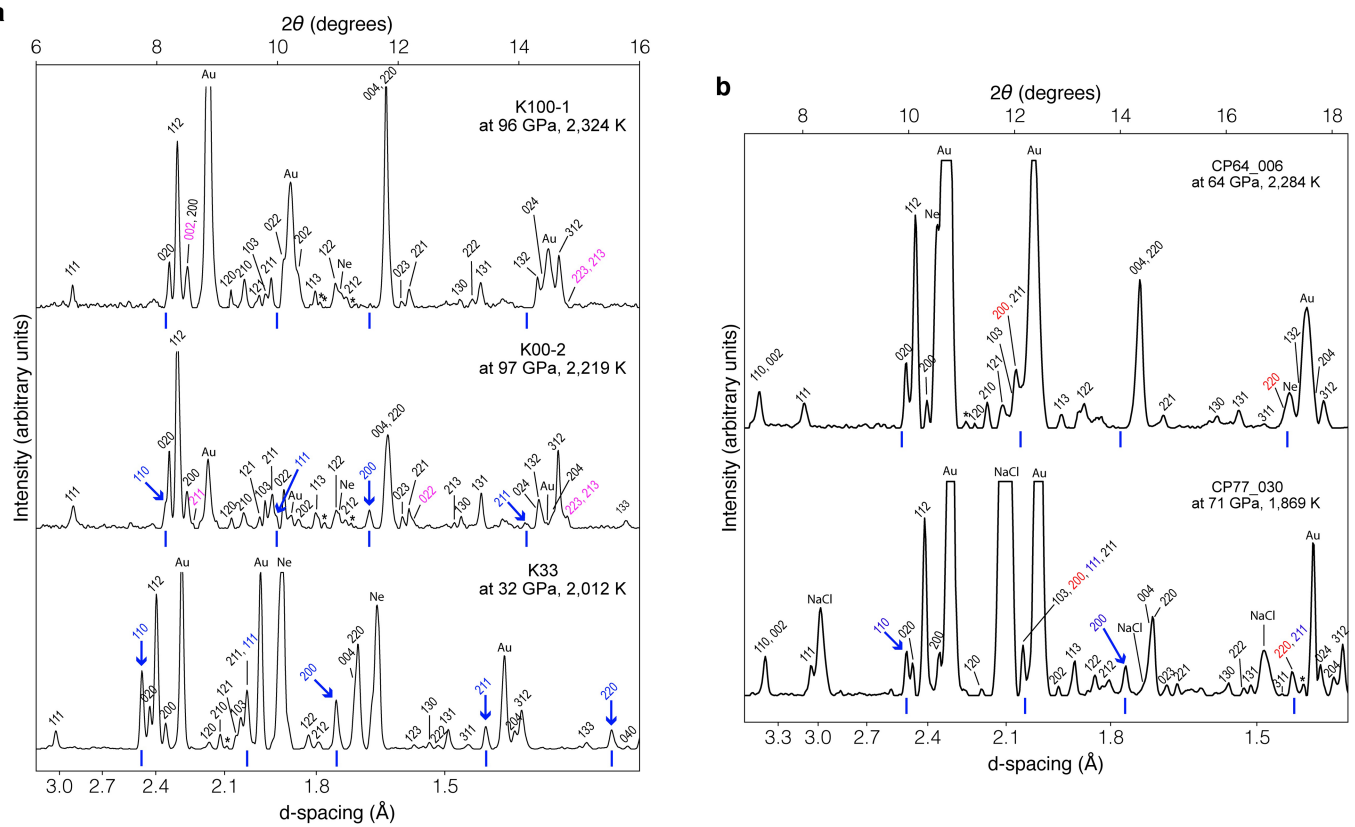
Reprints and permissions information is available at <http://www.nature.com/reprints>.

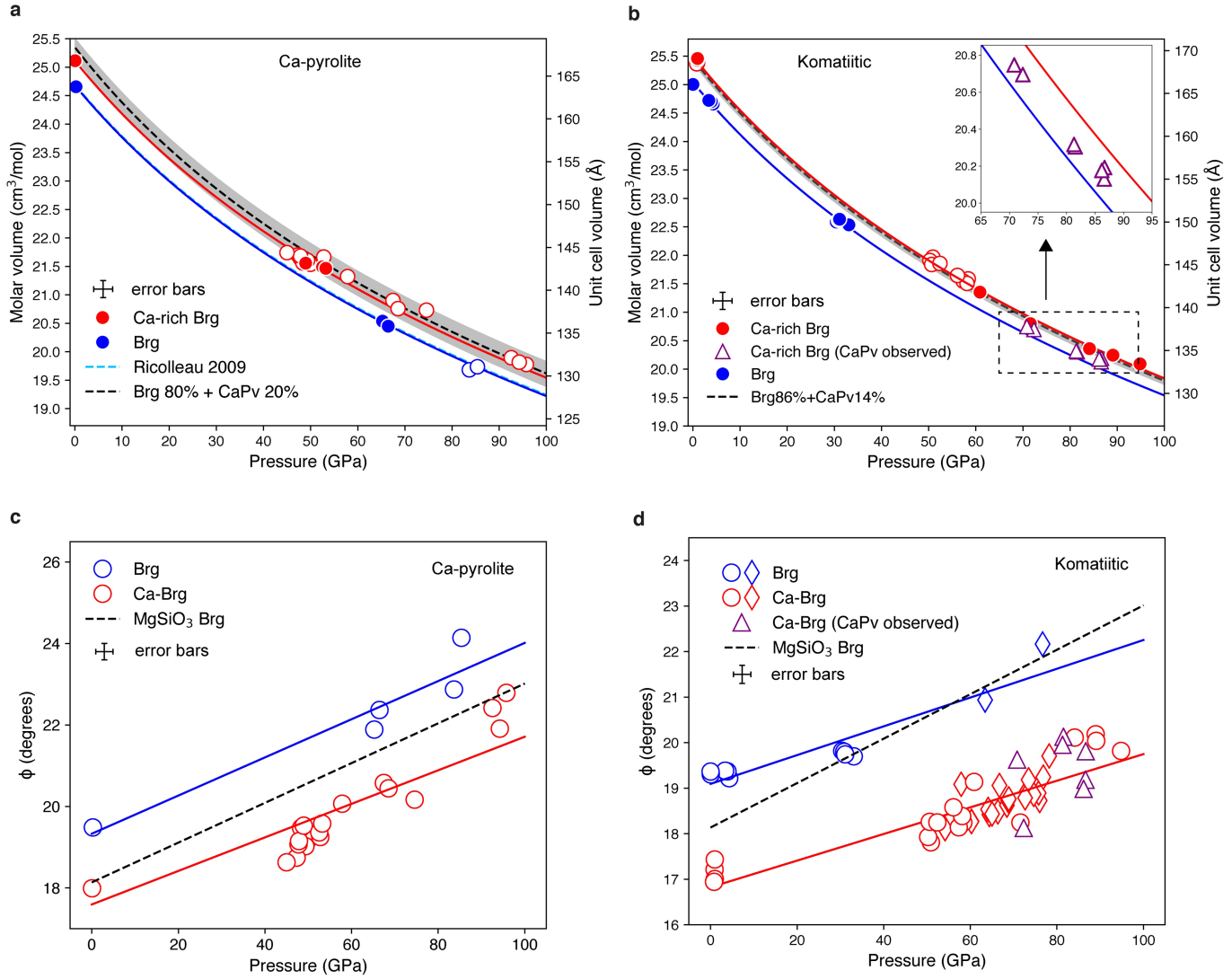


Extended Data Fig. 1 | Previous reports of existence (small symbols) or absence (large symbols) of CaSiO₃ perovskite from experiments on pyrolytic and peridotitic compositions. The data are collected from refs. ^{2,3,6–8,28,48–59}.

Mantle geotherms are shown as a grey area with the lower bound from ref. ⁴, and the upper bound from ref. ⁵. Diamonds: bridgmanite + ferropericlase + CaSiO₃

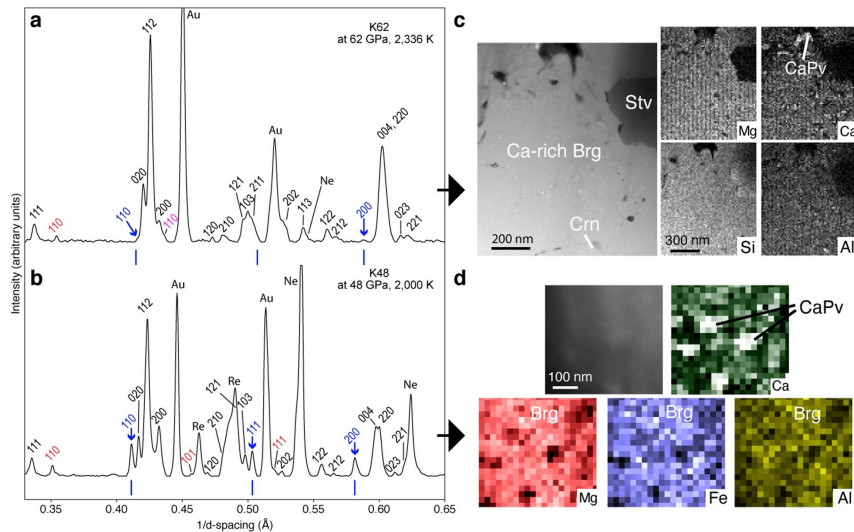
perovskite. Circles: bridgmanite + ferropericlase or bridgmanite only. Squares: bridgmanite (+ post-perovskite) + ferropericlase + CaSiO₃ perovskite. Pentagons: bridgmanite (+ post-perovskite) + ferropericlase. The open symbols are from this study.





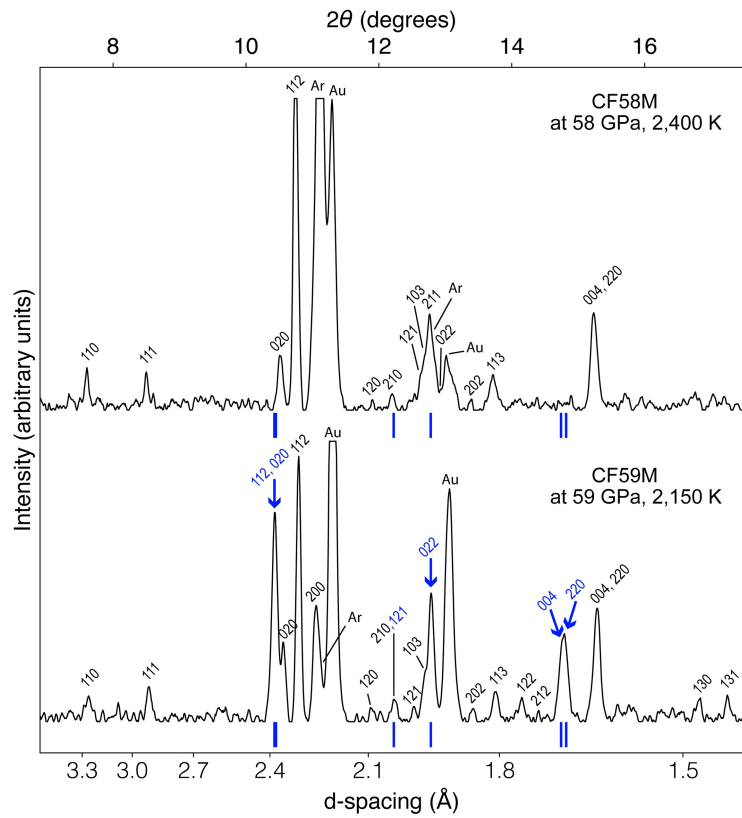
Extended Data Fig. 3 | Effects of Ca dissolution on crystal structure of bridgmanite. **a,b**, The molar volumes of bridgmanite (Brg) at high pressures and 300 K. The red and blue symbols represent Ca-rich Brg and Brg, respectively. The solid curves are fits of the solid symbol data points to the Vinet equation with fixed $K_0' = 4$. The data shown as open symbols were not used for fitting. The calculated molar volume of the Brg + CaSiO_3 perovskite (CaPv) assemblage is plotted as the dashed black curve for comparison with uncertainties (the grey shade). **a**, The blue dashed curve is from Mg,Fe,Al-bearing Brg in KLB-1 peridotite².

b, The inset is a magnified view for the purple triangles. **c,d**, The octahedral tilting of Brg at high pressures and 300 K. The octahedral tilting angle for MgSiO_3 endmember Brg is shown as the black dashed line. **d**, The red circles (K62 and K100) and diamonds (K59B and K73B) denote Ca-rich Brg. The blue circles (K33) and diamonds (K59B and K73B) denote Brg. **b,d**, The purple triangles represent the data points of Ca-rich Brg observed together with CaPv in XRD patterns (K100-2; Methods). The error bars are estimated to uncertainties.

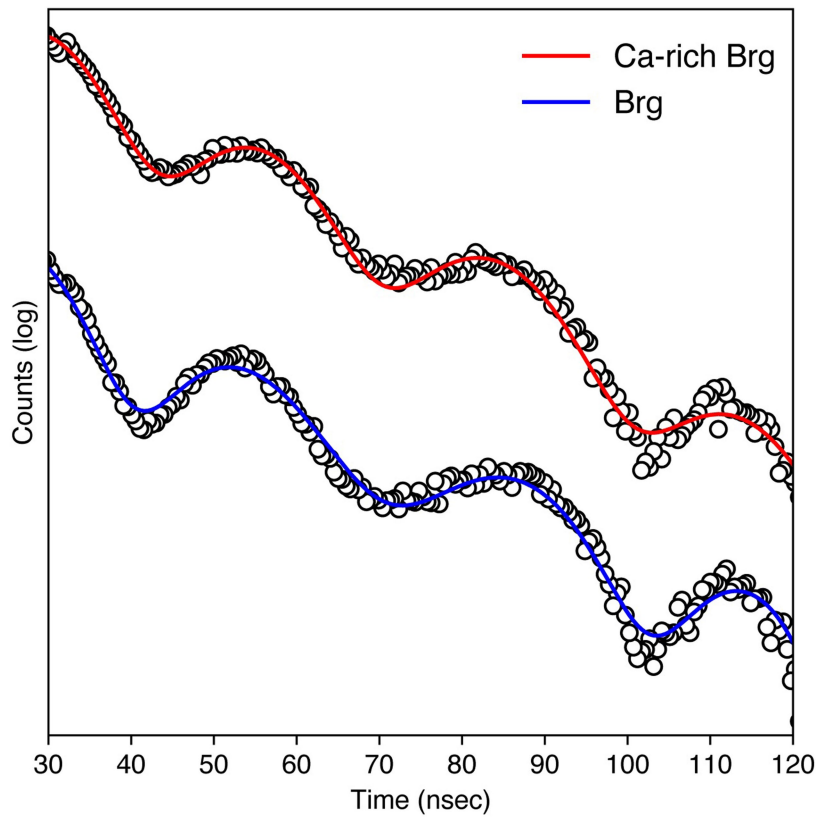


Extended Data Fig. 4 | X-ray diffraction patterns and chemical analysis of komatiitic composition synthesized at 62 GPa and 2,350 K (K62) and 48 GPa and 2,000 K (K48). **a,b**, Miller indices of Ca-rich bridgemanite (Brg), CaSiO₃ perovskite (CaPv), stishovite (St), and corundum (Crn) are provided as the black, blue, red, and magenta labels, respectively. The expected diffraction peak positions of CaPv are shown as the blue bars. **c,d**, A high-angle angular

dark-field image (left) and chemical maps (right) of the recovered samples. A small grain of CaPv is rarely observed in **c**, as the majority of Ca exists in Ca-Brg because of an increase in Ca solubility in Brg with temperature. However, at lower temperature CaPv is frequently observed because of low Ca solubility in Brg at the conditions.

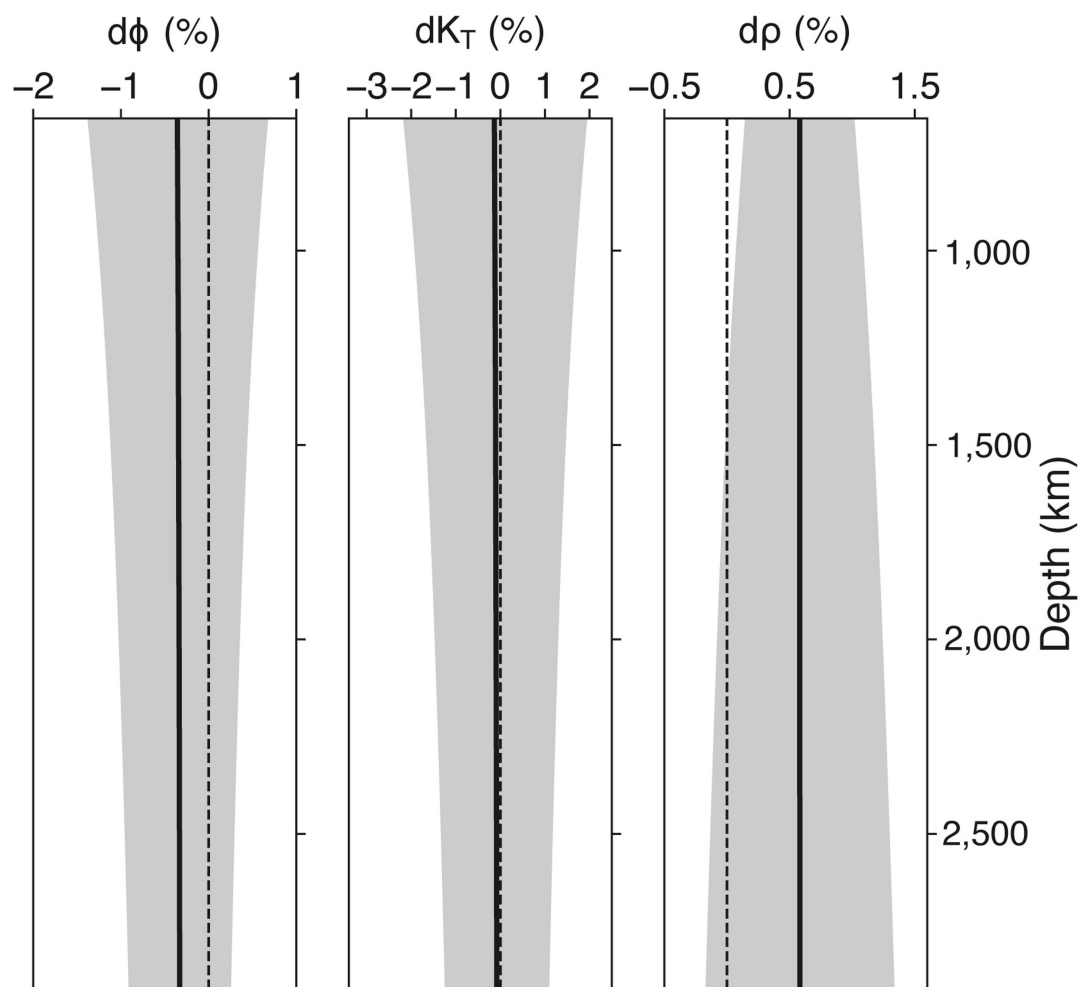


Extended Data Fig. 5 | X-ray diffraction patterns of the $\text{Ca}_{30}\text{Fe}_{13}$ composition at high pressures and 300 K. Pressures were measured at 300 K after heating. The Miller indices of bridgemanite and CaSiO_3 perovskite are provided as the black and blue labels, respectively. The expected diffraction peak positions of CaSiO_3 perovskite (tetragonal, space group: I4/mcm) are shown as the blue bars.



Extended Data Fig. 6 | Synchrotron Mössbauer spectra of bridgmanite (Brg) and Ca-rich Brg at 59 GPa and at 58 GPa after laser heating. The synthesis temperatures were 2,150 K and 2,400 K for Brg and Ca-rich Brg,

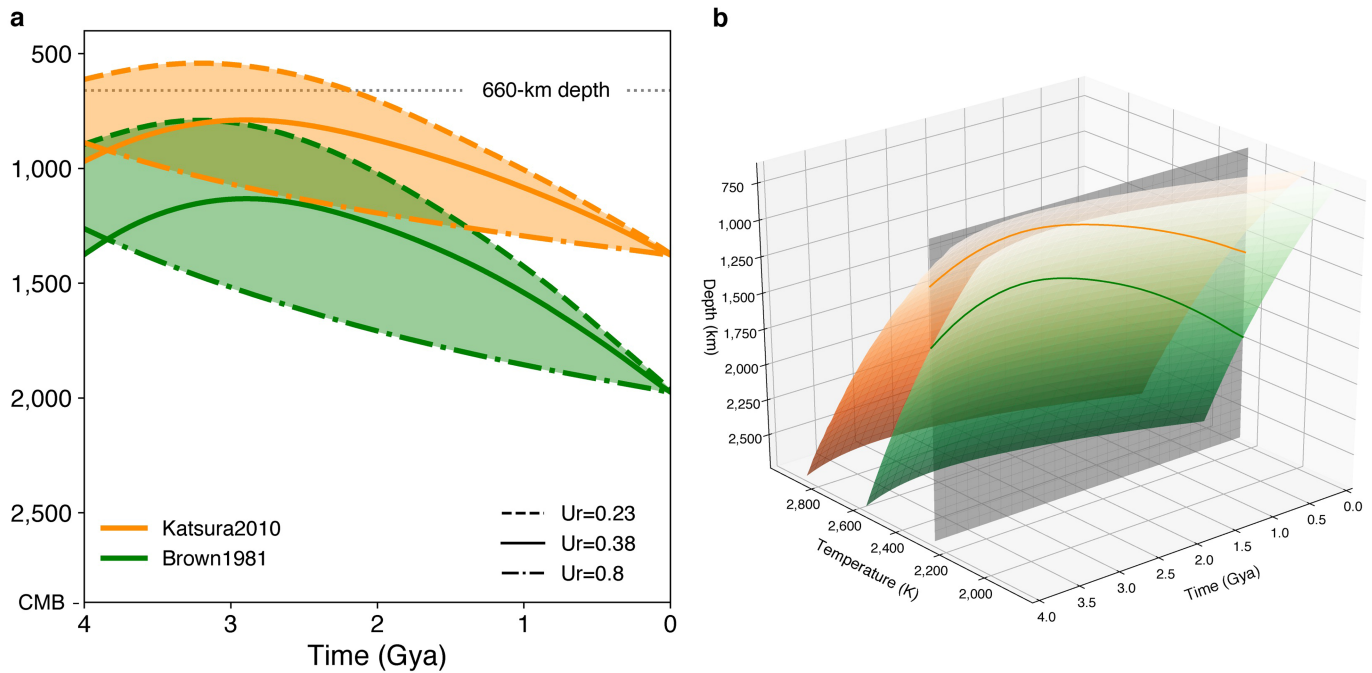
respectively. The circles are measured spectral data points and the curves are spectral fitting results.



Extended Data Fig. 7 | Differences in the seismic properties between the single-perovskite phase (Ca-rich bridgmanite) case and the two perovskite phases (bridgmanite + CaSiO₃ perovskite) case. The differences of Ca-rich

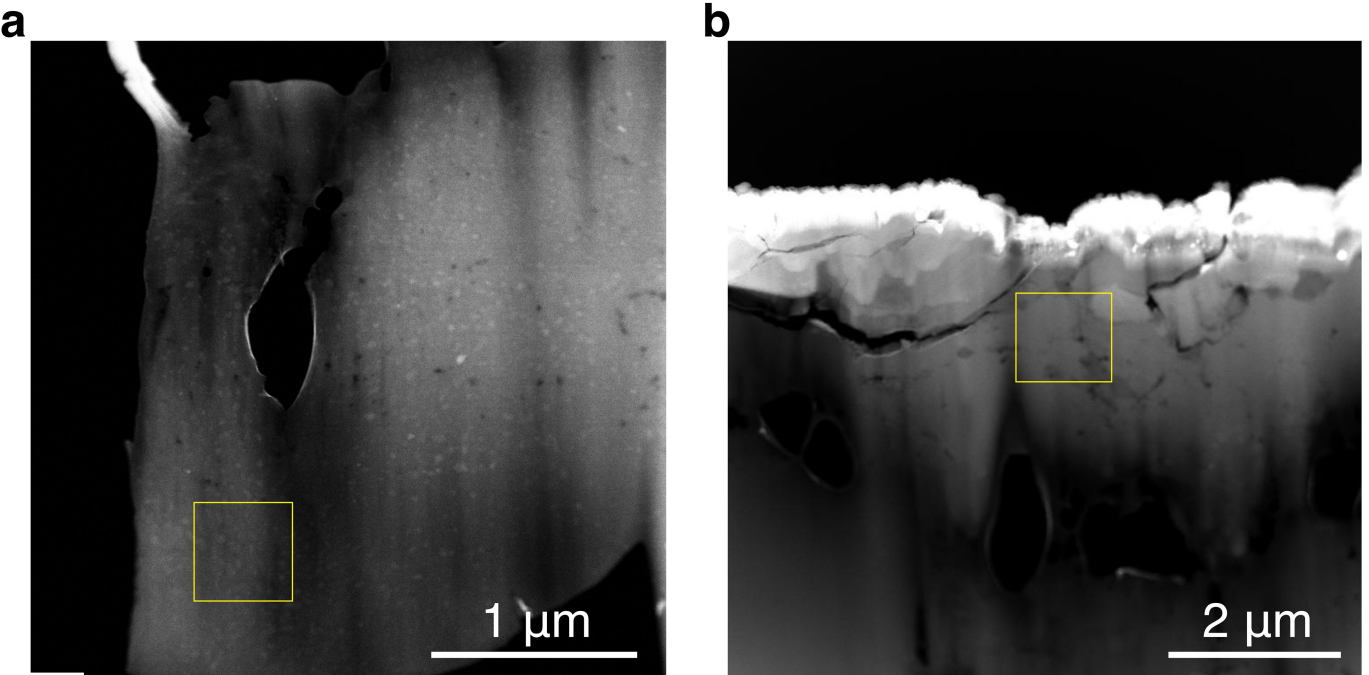
bridgmanite from bridgmanite + CaSiO₃ perovskite are shown for bulk sound speed (Φ), bulk modulus (K_T), and density (ρ) for the komatiitic composition at 300 K. The grey shades show the estimated 1σ uncertainties.

Article



Extended Data Fig. 8 | The depth of the transition zone from a two-perovskite domain (TPD; bridgmanite + CaSiO_3 perovskite) at shallower depths to a single-perovskite domain (SPD; Ca-rich bridgmanite) at greater depths over time in the lower mantle. a, The depth of the TPD-to-SPD transition zone (TSTZ) was calculated for the mantle geotherms from ref.⁴

(green) and ref.⁵ (orange) for Urey ratios (Ur) of 0.23, 0.38 (ref.²⁵) and 0.8 (ref.²⁶). The thickness of the TSTZ was not considered for the calculation. **b,** A 3-D plot of the TSTZ depths for Ur = 0.38. The green and orange planes intersect the grey plane which represents the TSTZ at 2,300 K.



Extended Data Fig. 9 | High-angle annular-dark-field images of the samples of Ca-pyrolite (a) and komatiitic composition (b). **a,b**, The yellow boxes indicate the areas where chemical compositions were measured, which are presented in Fig. 2b, d. **a**, Chemical compositions were analysed at the bottom left of the sample where the thickness was smaller. The presented area of the sample shows texture consistent with heating centre, that is, well crystallized

bridgmanite and ferropericlase. **b**, Chemical compositions were analysed at the top area of the sample. The Ca-rich bridgmanite matrix is nearly indistinguishable from the unheated glass since the Ca-rich bridgmanite matrix takes roughly 95 vol% of the sample. However, the well crystallized grains of other phases (Al_2O_3 and SiO_2) show that the area is well heated.

Article

Extended Data Table 1 | Chemical compositions of the starting materials (mol%)

Components	Ca-pyrolite	Komatiitic	Ca10Fe10	Ca30Fe13
SiO ₂	41.2(2)	44.1(1)	50.0(2)	46.9(2)
Al ₂ O ₃	2.2(0)	4.2(1)	NA	0.2(0)
FeO	4.6(1)	9.9(3)	5.0(1)	6.5(2)
MgO	43.0(2)	31.8(1)	40.0(2)	31.7(1)
CaO	9.1(5)	8.8(1)	5.0(1)	14.7(7)
Na ₂ O	NA	1.2(1)	NA	NA

For Ca-pyrolite, we added CaSiO₃ to the pyrolite composition from ref. ¹³. The komatiitic composition was obtained from ref. ³⁴.

Extended Data Table 2 | Fitting results for synchrotron Mössbauer spectroscopy for Ca₃₀Fe₁₃ composition at high pressure and 300K

Run	Phase	Pressure (GPa)	Site	wt%	IS (mm/s)	QS (mm/s)
CF58M	Ca-rich Brg	58	Fe ²⁺ #1	27.3	0.84	2.42
			Fe ²⁺ #2	17.3	0.79	2.85
			Fe ³⁺	55.5	0.28	1.82
CF59M	Brg + CaPv	59	Fe ²⁺ #1	44.2	0.73	2.48
			Fe ²⁺ #2	10.3	0.99	3.25
			Fe ³⁺	45.5	0.14	1.73

IS: isomer shift; QS: quadrupole splitting. Isomer shift values of CF58M and CF59M are calibrated to FeSO₄·7H₂O and stainless steel, respectively. The uncertainties of the values are less than 3%.

Article

Extended Data Table 3 | Summary of the experimental runs

Composition	Runs	Beamline	λ (Å)	Medium	P scale	P (GPa)	T (K)	# of heating spots	Analysis
Ca10Fe10	CF40	13-IDD	0.4133	NaCl	Au	39-42 (3)	1807-2526 (119-144)	4	Stab.
Ca-pyrolite	CP57	13-IDD	0.4133	Ne	Au	51-63 (4)	2343-2592 (124-266)	3	Stab.
	CP64	13-IDD	0.4133	Ar	Au	64 (4)	2284 (254)	1	Stab., EOS, Chem.
	CP65	13-IDD	0.4133	NaCl	Au	61-68 (4-5)	2123-2909 (103-181)	3	Stab.
	CP77	13-IDD	0.4133	NaCl	Au	71-83 (5-6)	1869-3022 (123-313)	6	Stab., EOS
	CP100	13-IDD	0.4133	NaCl	Au	90-107 (6-7)	1932-2861 (129-224)	6	Stab.
	K33	13-IDD	0.3344	Ne	Au	33 (2)	2200 (200)	3	Stab., EOS, Chem.
Komatiitic	K48	16-IDB	0.4066	Ne	Au	48 (3)	2000 (200)		Stab, Chem.
	K62	13-IDD	0.3344	Ne	Au	62 (4)	2350 (350)		Chem.
		16-IDB	0.4066						
	K100	13-IDD	0.3344	Ne	Au	100 (7)	2300 (150)		Stab., EOS, Chem.
		16-IDB	0.4066						
	K59B	13-IDD	0.3344		Brg, CaPv	55-69 (6-7)	2000-2700 (100-129)	12	Stab.
Ca30Fe13	K73B	13-IDD	0.3344		Brg, CaPv	76-82 (8)	2027-2570 (100-152)	12	Stab.
	CF58M	13-BMC	0.4340	Ar	Au	58 (2 at 300K)	2400 (100)		M.S.
		3-IDB							
	CF59M	13-BMC	0.4340	Ar	Au	59 (2 at 300K)	2150 (300)		M.S.
		3-IDB							

The CF58M and CF59M samples were synthesized at ASU. λ : X-ray wavelength; P: pressure; T: temperature; Brg: bridgmanite; CaPv: CaSiO_3 perovskite; Stab.: examination of stability; EOS: equation of state; Chem.: chemical analysis; M.S.: Mössbauer spectroscopy.